frontiers in Earth Science

ORIGINAL RESEARCH
published: 22 March 2022
doi: 10.3389/feart.2022.842386

Fluid Inclusion, Isotopic, and Elemental Geochemistry Studies of Cave-Filling Calcite in the Lower–Middle Ordovician Yingshan Formation of Tahe Oilfield, NW China: Implication for Karstification in Non-exposed Limestone

Yongmei Zhang[1,2], Shaonan Zhang[3], Baiwen Huang[3]*, Ziye Lu[3], Ning Ye[3], Bei Zhu[3], Xianhai Hou[4], Fei Xie[4], Xiaoliang Bai[5] and Xinyan Zhang[5]*

[1]State Key Laboratory of Oil and Gas Reservoir Geology and Exploitation, Chengdu University of Technology, Chengdu, China, [2]College of Energy Resource, Chengdu University of Technology, Chengdu, China, [3]School of Geoscience and Technology, Southwest Petroleum University, Chengdu, China, [4]Northwest Oilfield Company Sinopec, Urumqi, China, [5]Research Institute of Exploration and Development, PetroChina Southwest Oil and Gasfield Company, Chengdu, China

Improving the recognition of paleo-fluid circulation history is of great significance to reconstruct pore evolution during carbonate diagenesis. Integrated petrography, fluid inclusion, isotopic and elemental geochemistry (laser ablation inductively coupled plasma mass spectrometry) studies, calcites generated in paleocaves, and fractures were investigated. This study aims to reveal the paleo-fluid origin and karstification event within the nonexposed limestone of the Lower–Middle Ordovician Yingshan Formation in the Tarim Basin. The only generation of blocky calcite growing along the karst paleocave and fracture walls [cave-filling calcite (CFC)] crosscuts burial stylolites. The secondary fluid inclusions obtained from CFC are characterized by the coexistence of liquid-only and liquid-dominated aqueous inclusions with low salinities values (0–2.4 wt%), suggesting that the CFC has experienced a low-temperature environment (<50°C). The depleted $\delta^{18}O$ values (–15.32‰ to 12.45‰), seawater-like yttrium and rare earth element patterns, and low ΣREE (<0.65 ppm) have recorded the major episode of meteoric water leaching the Yingshan limestone. This view was further confirmed by the calculated $\delta^{18}O_{water}$ values of parent fluids (–14.3‰ to 2.2‰). The relatively higher $^{87}Sr/^{86}Sr$ ratios (0.70942–0.70994) are interpreted as the result of meteoric water interacting with the overlying Silurian detrital rock when percolated downward. The geochemical evidence recorded by CFC indicates that the karstification event for Yingshan nonexposed limestone possibly took place in the Early Hercynian period during the late Devonian. Therefore, meteoric water percolating downward along the fractures penetrating insoluble strata and/or migrating laterally along the permeable strata is deemed responsible for the karstification event, although the overlying thick insoluble strata in the coverage area.

Keywords: nonexposed limestone, paleocaves, carbon and oxygen isotopes, strontium isotopes, *in-situ* REE, meteoric water

OPEN ACCESS

Edited by:
Shu Jiang,
The University of Utah, United States

Reviewed by:
Lingtao Kong,
East China University of Technology, China
Jie Li,
China University of Geosciences Wuhan, China
Hairuo Qing,
University of Regina, Canada
Pei Shang,
East China University of Technology, China

****Correspondence:***
Shaonan Zhang
zsn@cdut.edu.cn
Baiwen Huang
1002871538@qq.com

Specialty section:
This article was submitted to Economic Geology, a section of the journal Frontiers in Earth Science

Received: *23 December 2021*
Accepted: *27 January 2022*
Published: *22 March 2022*

Citation:
Zhang Y, Zhang S, Huang B, Lu Z, Ye N, Zhu B, Hou X, Xie F, Bai X and Zhang X (2022) Fluid Inclusion, Isotopic, and Elemental Geochemistry Studies of Cave-Filling Calcite in the Lower–Middle Ordovician Yingshan Formation of Tahe Oilfield, NW China: Implication for Karstification in Non-exposed Limestone. Front. Earth Sci. 10:842386. doi: 10.3389/feart.2022.842386

INTRODUCTION

It has been known that considerable hydrocarbon resources (approximately 40% or more) are trapped at carbonate reservoirs (Sayago et al., 2012). Some hydrocarbon reservoirs with significant production may be paleokarst origin such as the Lower to Upper Paleozoic carbonates in the west Texas (Kerans, 1988), and the Ordovician carbonates in the Ordos and Tarim basins (Fu et al., 2012; Tian et al., 2016). The paleokarst processes ranging from near-surface corrosion to deep-buried dissolution have influenced numerous carbonate reservoirs that host petroleum accumulation (Loucks, 1999; Sayago et al., 2012; Lønøy et al., 2021). Most paleokarst-related carbonate reservoirs are considered to originate from near-surface karst processes related to stratigraphic unconformity and subsequently subjected to further burial dissolution (Sayago et al., 2012).

According to the published researches, near-surface karst reservoirs are formed from dissolution by carbonate unsaturated fluids, such as freshwater (Raeisi and Mylroie, 1995; Zhang et al., 2017) or mixture of freshwater and seawater (Mylroie and Mylroie, 2007; Menning et al., 2015). Meanwhile, the paleokarst reservoirs are controlled by precursor mineralogy, grain size, initial porosity and permeability of the affected rocks, climate, and duration of

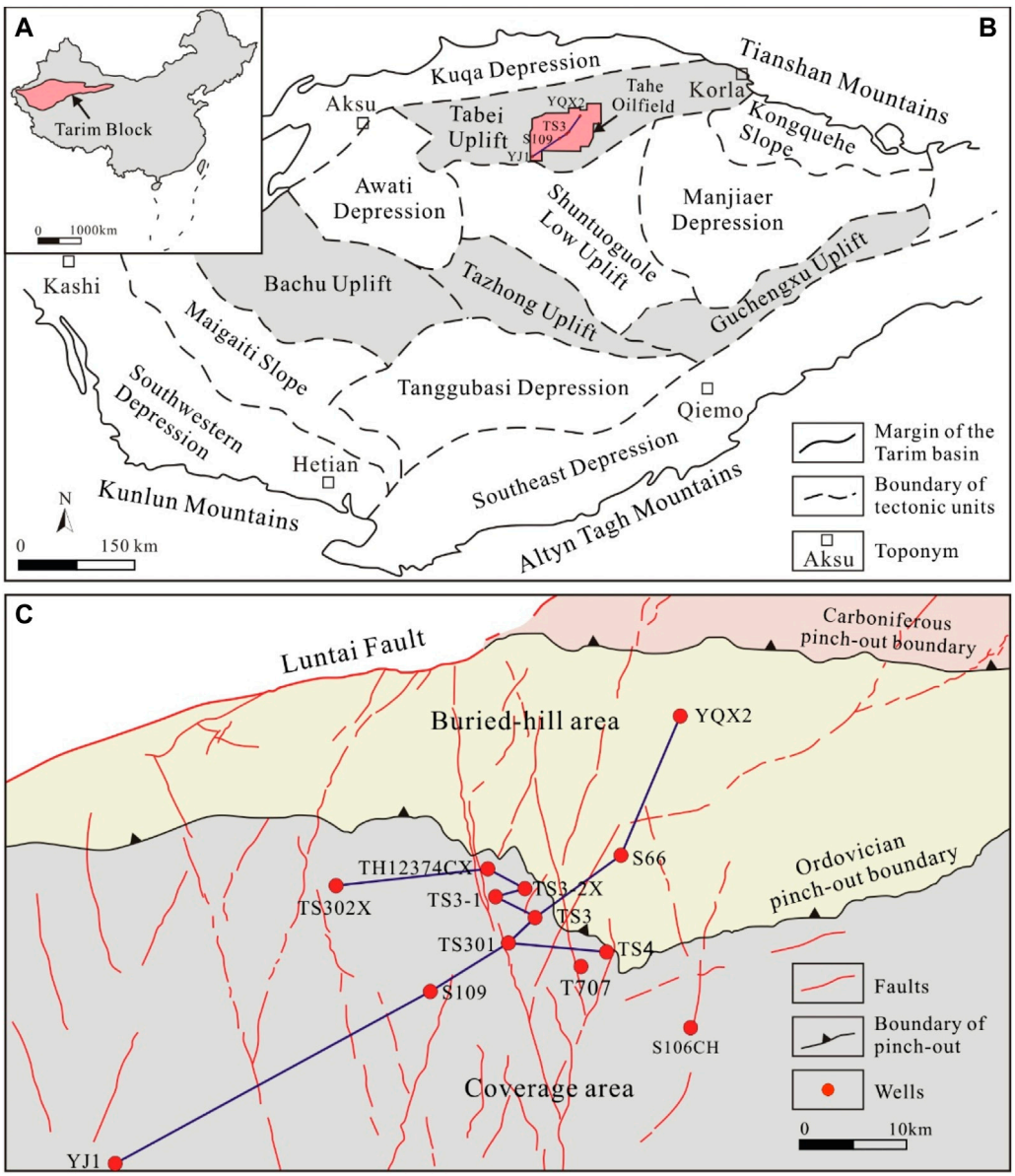

FIGURE 1 | (A) The location of the Tarim Basin in China. The red area signifies the Tarim Basin. **(B)** The location of the Tahe Oilfield in the Tarim Basin. The red area indicates the Tahe Oilfield. **(C)** The location of the wells and faults in the Tahe Oilfield. The gray area indicates the coverage area in the Tahe Oilfield. The yellow and red areas indicate the buried-hill area.

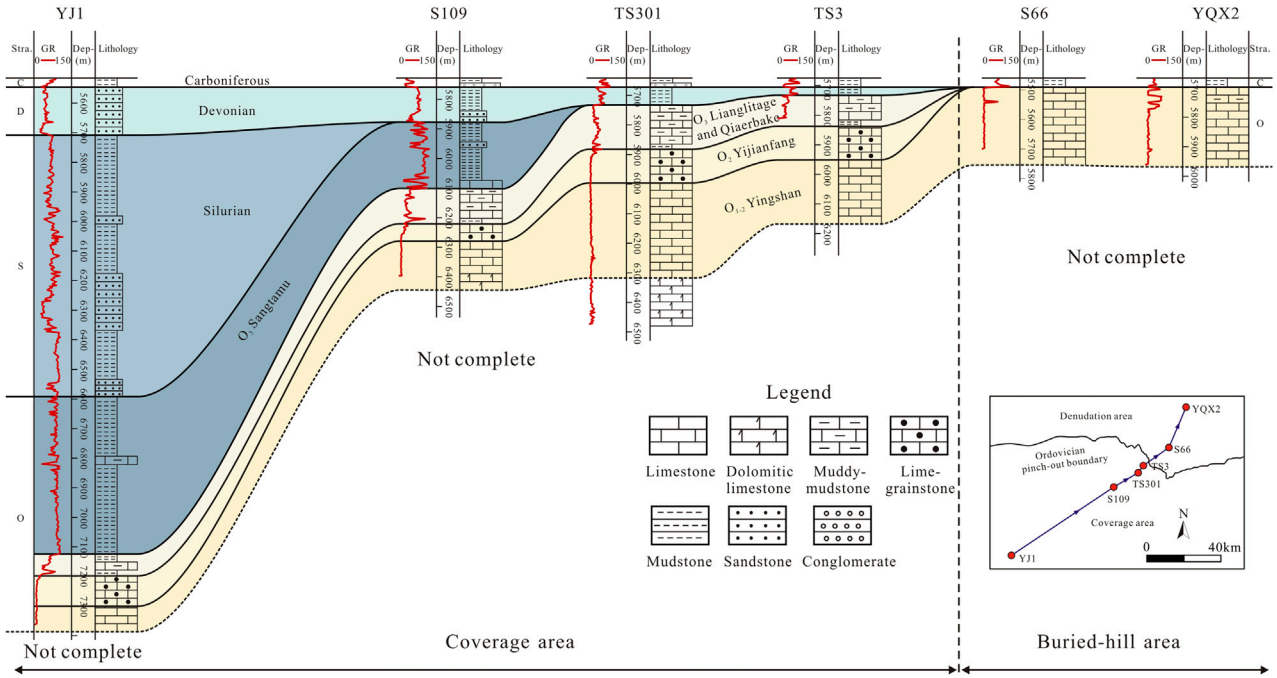

FIGURE 2 | Cross section of the Tahe area shows different formation contacts in the south to north.

exposure (Loucks, 1999). However, it is difficult to reveal freshwater activities in the deep-buried carbonate due to limited cores. Geochemical signatures of calcites are proved to be useful tools that can help to identify the karst processes. Some researchers have classified paleokarst stages by carbon, oxygen, and strontium isotopic compositions (Ainsaar et al., 2010; Han et al., 2019), and the others have distinguished the fluid origin according to the fluid inclusion analyses (Rossi et al., 2002). Moreover, interest in yttrium and rare earth elements (REEYs) has emerged, which shows the potential as paleoclimatic and paleohydrological proxies (Bourdin et al., 2011). Therefore, integrated applications of petrography, geochemistry, and fluid inclusion studies of cave-filling calcites (CFCs) can assist in deciphering the paleokarst reservoirs origin.

The Tarim Basin covered an area of approximately 56×10^4 km^2 (**Figure 1A**) and is the largest hydrocarbon-bearing basin in China in terms of area (Chen et al., 2012). The Tahe Oilfield located in Tabei Uplift is the largest known Palaeozoic marine carbonate oil field in China (Lu X et al., 2017). The most important pay layer of the Tahe Oilfield is the freshwater-leaching Ordovician carbonate, and the proved reserves of crude oil are estimated to be 5.875×10^8 tons in the Ordovician paleokarst carbonate reservoirs (Han et al., 2019).

In the northern part of the Tahe Oilfield (or "buried-hill area"), mega-paleokarst systems developed in the Lower to Middle Ordovician limestone (the Yingshan limestone). The Yingshan limestone has undergone two stages of significant karstification during the Middle Caledonian and Early Hercynian periods. In the southern part of the Tahe Oilfield (or "coverage area") (**Figure 2**), the Yingshan limestone is covered by the Middle Ordovician limestone and the Upper Ordovician lime-mudstone and muddy limestone with a thickness of more than 220 m. Therefore, the paleokarst reservoirs are generally considered to be less developed than those in the buried-hill area (Yang et al., 2014). However, the phenomenon of blowdown and leakage during drilling is also common in the Yingshan limestone of the coverage area, implying the development of paleokarst reservoirs.

The Yingshan limestone has recently made significant oil achievements at a depth more than 6,000 m in the coverage area (Lu Z et al., 2017). It has been evidenced that the hydrocarbon reservoirs in buried-hill area were dominated by Early Hercynian karstification during the late Devonian period (Gao et al., 2020; Zhang et al., 2021). However, controversy still remains regarding the generation of the hydrocarbon reservoirs in coverage area. Some researchers have emphasized that the paleokarst reservoirs were generated by the Middle Caledonian karstification during the late Middle Ordovician, because of the influence of paleogeomorphology and overlying Middle to Upper Ordovician insoluble strata (Yang et al., 2014). On the contrary, some scholars stressed that the Middle Caledonian karstification was characterized by contemporaneous karst based on the conodont biostratigraphy, which made it impossible to generate large-scale paleokarst reservoirs (Lv et al., 2009). Others proposed that the karst-fault paleokarst reservoirs were developed by input of dissolution fluids along the fractures (Lu et al., 2017; Han et al., 2019; Méndez et al., 2019). These debates indicate that the hydrocarbon reservoirs in the coverage area have not been adequately studied. Meanwhile, these analyses were not constrained by elements, isotope ratios, and/or fluid inclusion

evidence, casting doubt on the fluid origin. Therefore, identifying fluid origin of the paleokarst reservoirs in the coverage area can greatly improve the further exploration in the Tahe Oilfield.

In this study, based on petrography, isotopic compositions, fluid inclusion studies, and *in situ* REEY analysis of CFC, the main objectives of this article are to (1) characterize the paleocave distribution features and discuss the parent fluid origin of CFC and (2) reconstruct the karstification model for nonexposed paleokarst carbonate reservoirs. The results provide a pioneering research for the evaluation of paleokarst reservoirs in nonexposed carbonate and guide further hydrocarbon exploration in deep-buried carbonate.

GEOLOGICAL BACKGROUND

The Tarim Basin as a composite superimposed basin developed on the pre-Sinian basement (Jia et al., 1998) is the largest productive basin situated in the northwest China (**Figure 1A**). Situated on the northwest of the Tarim Basin (**Figure 1B**), the Tabei Uplift is tectonically bounded by the Kongquehe Slope, Manjiaer Depression and Shuntuoguole Low Uplift in the southeast, Awiti Depression in the southwest, and Kuqa Depression in the northwest. The Tahe Oilfield (the study area), which encompassed an area of 2,400 km^2, is located in the southeast of Tabei Uplift (**Figure 1B**).

More than 10,000-m thickness of sediments developed in the study area, including the Cambrian-Ordovician marine carbonates and the Silurian-Quaternary marine–terrestrial clastic strata (Sun et al., 2013). The Ordovician strata consist of, in an ascending order, the Lower Ordovician Penglaiba (O_1p), the Lower–Middle Ordovician Yingshan ($O_{1\text{-}2}y$), the Middle Ordovician Yijianfang (O_2yj), the Upper Ordovician Qiaerbake (O_3q), and Lianglitage (O_3l) and Sangtamu (O_3s) formations (**Figure 2**). The sedimentary face was restricted platform in the Early Ordovician (Gao and Fan., 2015) and then transformed to open platform as a result of tectonic movement and sea level variation during the Middle Ordovician in the Tabei area (Gao et al., 2006a). In the Late Ordovician, a large-scale transgression submerged the carbonate platform, and the sedimentary face was converted into deep-water shelf and basin. Therefore, the carbonate deposition was much reduced and gradually evolved into a mixed carbonate-siliceous clastic sedimentary system (Gao et al., 2006b; Feng et al., 2007; Gao and Fan, 2015). The marine carbonates are dominated by dolostones from the Cambrian to the Lower Member of the Yingshan Formation and mainly comprise limestone in the Upper Member of the Yingshan Formation and the Yijianfang Formation. The Upper Ordovician strata mainly comprise mudstones, sandstone, marl, and nodular limestone, which are the regional cap rocks in the Tabei area.

The Tarim Basin has experienced intense multistage tectonic movements in Paleozoic period and ranges from extensional to compressional environment since the Early Ordovician (Jia et al., 1998), due to the closure of the North Kunlun Ocean and the Altyn Ocean. This tectonic movement had a significant influence on the Bachu Uplift and Tazhong Uplift, resulting in a partial or total absence of the Middle and Upper Ordovician strata (Tian et al., 2020). However, it had slighter influence on the Tabei Uplift, which led to the development of the contemporaneous karstification in the Yijianfang and Lianglitage formations (Lv et al., 2009). During the Late Devonian to Early Carboniferous, the collision in the north edge of the Tabei Uplift resulting from the closure of the Tianshan Ocean is the most significant and influential stage, which leads to prolonged exposure and weathering (approximately 10 Ma) in the Tahe area (He et al., 2020). This uplift results in the intense unroofing and the absence of the Devonian, Silurian, and Middle-Upper Ordovician strata in the buried-hill area (**Figure 1C**), so that the Carboniferous strata unconformably overlie the Yingshan limestone in the north area of the Tahe area (**Figure 2**). In contrast, the coverage area experienced a relatively slighter uplift, so that the Devonian, Silurian, and Middle-Upper Ordovician strata were partially or completely preserved overlying the Yingshan limestones (**Figures 1C**, **2**). In addition, numerous reverse and strike slip faults are well developed during long-term and multistage tectonic activities (**Figure 1C**).

The Yingshan limestone experienced various degrees of karstification as a result of different structural thrusting and uplift in the study area. The karstification reservoirs are well-developed related to stratigraphic unconformities in the buried-hill area, whereas these were less developed in the coverage area because of the overlying insoluble strata. However, the blowdown and leakage during the drilling processes are still widespread in Yingshan limestone of the coverage area. The height of the blowdown section extends for several meters and up to 15 m in the Well of TS4 (**Figure 3**). The blowdown sections are distributed in the range of 170–200 m from the top of Yingshan Formation, indicating that the paleocaves are inferred to be layered distribution.

METHODS

Thirty-four samples were collected from the Yingshan Formation for petrographic analysis, and these sample distributions are shown in **Figure 3**. CFC samples were doubly polished into thin section approximately 90 μm thick for fluid inclusion petrography and microthermometry analysis. Cathodoluminescence microscopy was carried out on a RELITRON III stage in the state Key Laboratory of Oil and Gas Reservoir Geology and Exploitation, Southwest Petroleum University, using a gun current of approximately 0.3–0.5 mA and an acceleration voltage of 5–8 kV.

The fluid inclusion microthermometry was measured in CFC samples at Key Lab of Sichuan Province Natural Gas Geology, Southwest Petroleum University. Fluid inclusions were performed using a Linkam THMGS600 heating–freezing stage, which was calibrated using synthetic fluid inclusions with known compositions. The cycling technique proposed by Goldstein and Reynolds (1994) was used to measure homogenization temperatures (T_h) and ice final melting temperatures ($T_{m\text{-}ice}$) in this study. The precision of the heating, cooling, and/or cycling intervals are 0.1°C for $T_{m\text{-}ice}$ when the temperature is higher than

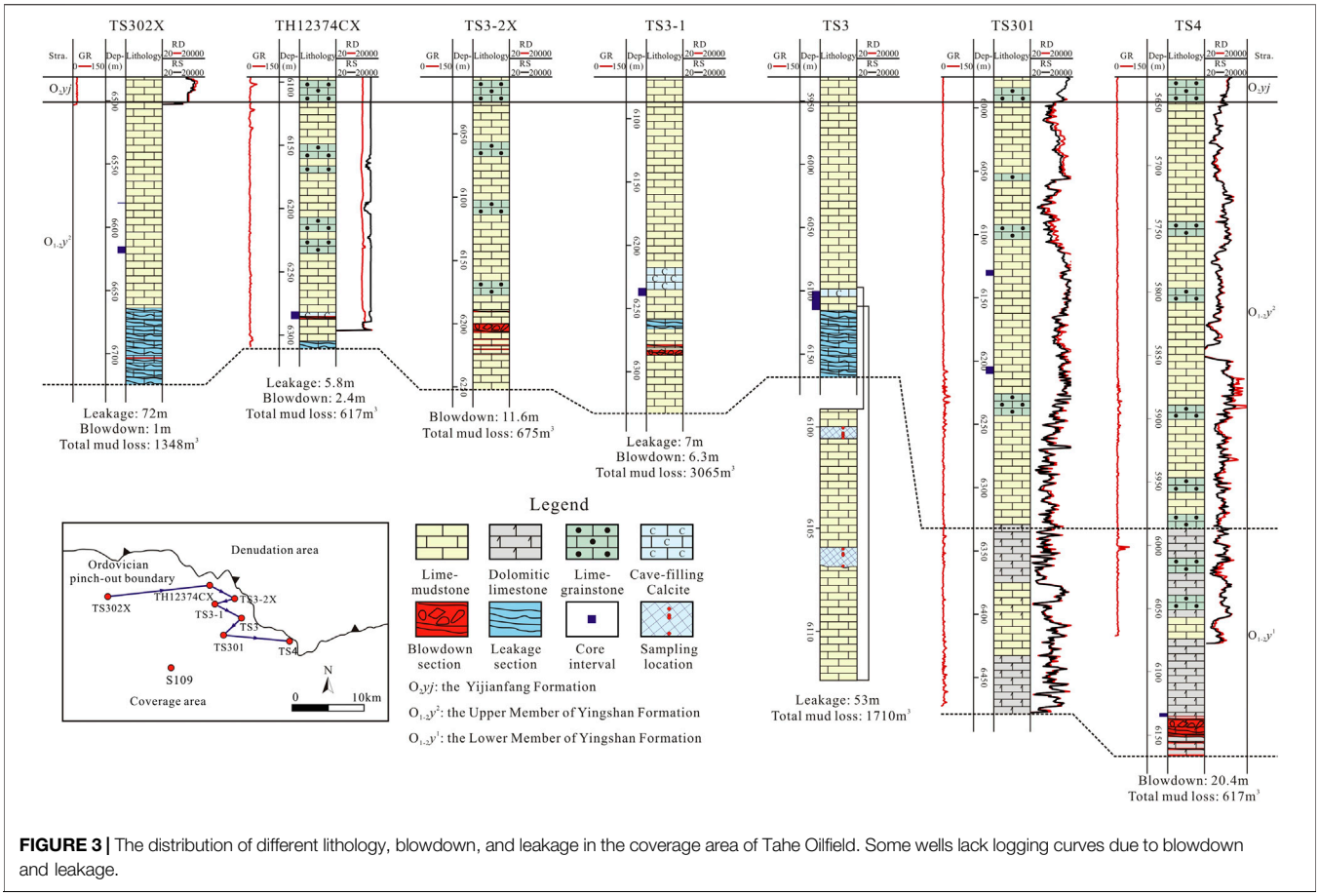

FIGURE 3 | The distribution of different lithology, blowdown, and leakage in the coverage area of Tahe Oilfield. Some wells lack logging curves due to blowdown and leakage.

−3°C, 1°C for $T_{m\text{-}ice}$ when the temperature is lower than −3°C, and 5°C for T_h and metastable freezing temperature (T_f). The liquid-only aqueous inclusions were stretched for $T_{m\text{-}ice}$ measurement by heating in a muffle furnace at 220°C for approximately 6 h (Goldstein and Reynolds, 1994).

Aqueous fluid inclusions in relatively soft minerals such as calcite are easily reequilibrated in association with increased temperatures during deep burial (Goldstein and Reynolds, 1994; Ujiie et al., 2008). Therefore, the concept of the fluid inclusion assemblage (FIA) is adopted to evaluate the validation of T_h and $T_{m\text{-}ice}$ in fluid inclusions. The last melting phase of all the inclusions was ice during low-temperature microthermometric work. The salinity of the inclusions was calculated by $T_{m\text{-}ice}$, using the program of Steele-MacInnis et al. (2011), based on the H_2O-NaCl system in this research.

Thirteen CFC samples and five micrite limestone (MC) samples were prepared for stable carbon ($\delta^{13}C$), oxygen ($\delta^{18}O$), and strontium ($^{87}Sr/^{86}Sr$) isotopes. These isotope analyses were all conducted at the State Key Laboratory of Oil and Gas Reservoir Geology and Exploitation, Chengdu University of Technology. Carbon and oxygen isotopes were performed using a MAT 253 mass spectrometer, and isotopic data were reported in the standard notation relative to the Vienna Peedee Belemnite (VPDB). Analytical precision of carbon and oxygen isotopic values are both better than ±0.01%. In addition, the parent fluid $\delta^{18}O_{water}$ (SMOW) value is calculated by the O'Neil et al. (1969) oxygen fractionation equation ($(10)^3 \ln\alpha_{calcite\text{-}water} = 2.78 \times 10^6\, T^{-2} - 2.89$).

Approximately 100-mg sample powder was dissolved for strontium isotope analyses. The $^{87}Sr/^{86}Sr$ ratios measurement was performed on a MAT262 solid isotope mass spectrometer and normalized relative to the NBS987 standard. The average standard error was $(2\sigma) \pm 12 \times 10^{-6}$.

In addition, previously published datasets in buried-hill area of Tahe Oilfield were compiled to analyze the fluid origin of CFC (Liu et al., 2008; Li et al., 2011; Jin et al., 2015; Liu et al., 2016; Liu L et al., 2017; Han et al., 2019). The isotope ratios of CFCs derived from different sources (hydrothermal fluid, meteoric water, and seawater) were constrained based on comprehensive analysis of elements, isotopes, and/or fluid inclusions in the buried-hill area. These published data include 54 carbon and oxygen isotopes and 36 $^{87}Sr/^{86}Sr$ ratios. The collected $\delta^{13}C$ and $\delta^{18}O$ values are considered comparable because they have been normalized to VPDB with an accuracy of ±0.1‰. Besides, these published data are evaluated here to give insights into diagenetic fluids.

In situ trace elemental measurements of CFC were conducted on a combined ESL193UC laser ablation system (ArF 193-nm gas excimer laser) and an Agilent 7800 inductively coupled plasma mass spectrometry at the Laboratory of Carbonate Sedimentary and Diagenetic Geochemistry, Southwest Petroleum University.

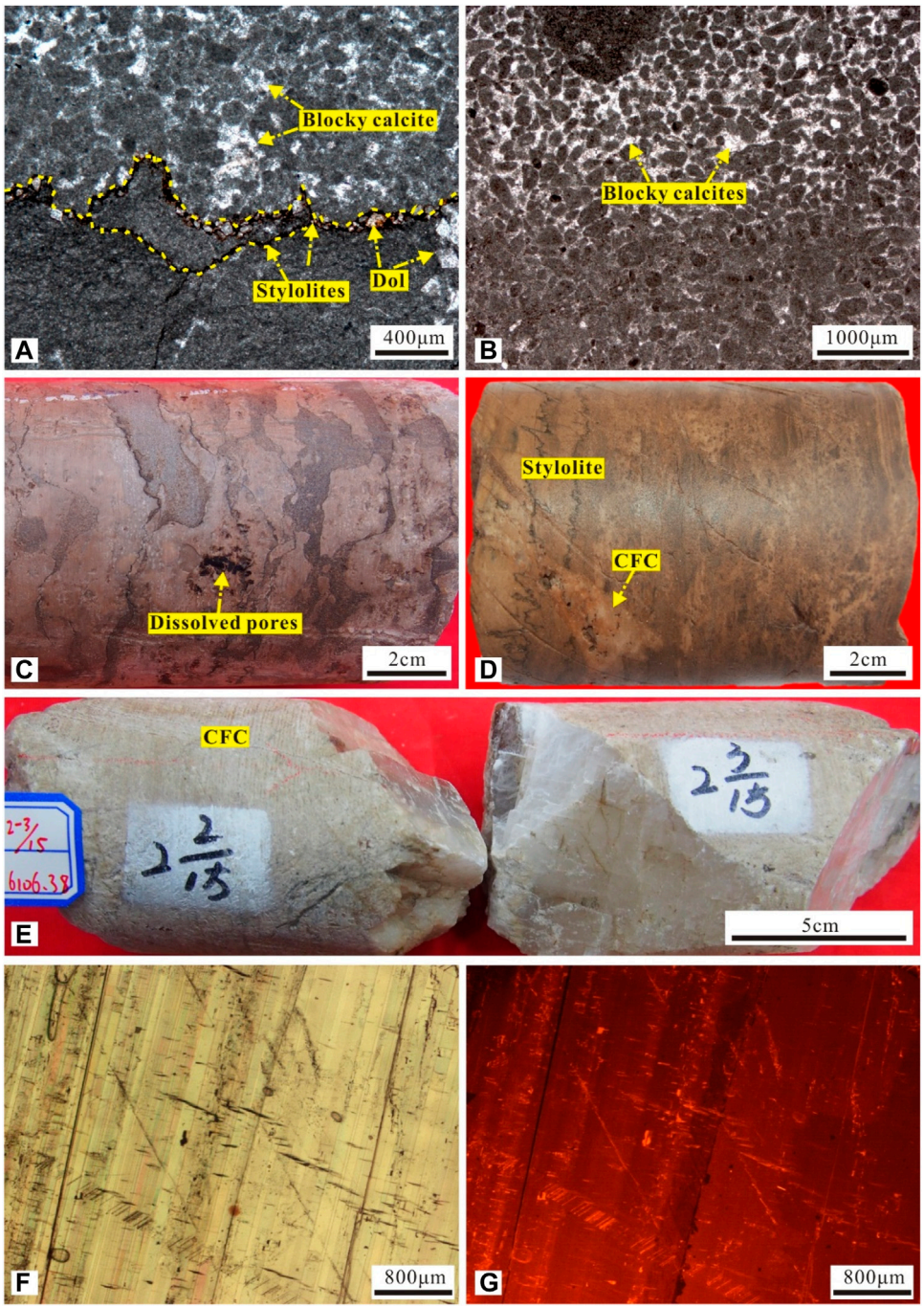

FIGURE 4 | Petrological characteristics of the matrix limestone and CFC. **(A)** Bedding-parallel stylolite represents at lithological transitional interface between lime-wackstone and lime-mudstone; subhedral dolomite scattered along the stylolites, together with residual bitumen, TS3, 6,239.05 m, $O_{1\text{-}2}y$. **(B)** Photograph of lime-wackstone and lime-packstone. The intergranular pores were completely filled by calcite cements, TS3-1, 6,239.62 m, $O_{1\text{-}2}y$. **(C)** Dissolved pores are partially filled with bitumen, TS3-1, 6,237.45–6,237.57 m, $O_{1\text{-}2}y$. **(D)** The fracture and related karstic reservoirs filled with CFC crosscut the stylolites, TS4, 6,133.0–6,133.12 m, $O_{1\text{-}2}y$. **(E)** Core photograph of blocky calcite filled in the paleocaves (CFC), TS3, 6,106.26–6,106.38 m, $O_{1\text{-}2}y$. **(F,G)** The CFC with a size more than 1,000 μm overall emits dull red to red luminescent, TS3, 6,106.20 m, $O_{1\text{-}2}y$.

The laser-spot size and frequency of the laser were set to 80 μm and 5 Hz, respectively, in this study. The standards NIST 612 and MACS-3 were used to correct for drift and check measurement uncertainties (Ca as internal standard; relative REE + Y concentration errors < 10%), respectively. Data processing and calibration were performed in Iolite (method from Paton et al.,

2011). The isotopes ^{89}Y, ^{139}La, ^{140}Ce, ^{141}Pr, ^{142}Nd, ^{148}Sm, ^{153}Eu, ^{157}Gd, ^{159}Tb, ^{163}Dy, ^{165}Ho, ^{166}Er, ^{169}Tm, ^{172}Yb, and ^{175}Lu were used to qualified REE + Y in the CFC samples. Some other elemental contents (^{27}Al, ^{55}Mn, ^{57}Fe, ^{88}Sr, and ^{91}Zr) were also measured to test for possible contaminants.

Raw REEY concentrations were normalized to Post-Archean Australian Shale (PAAS) (McLennan, 1989). The relative enrichments of the LREE, MREE (from Sm to Dy), and HREE fractions were evaluated by the ratios of $(Pr/Yb)_{SN}$, $(Pr/Tb)_{SN}$, and $(Tb/Yb)_{SN}$. The BSI (MREE enrichment) value is calculated following Tostevin et al. (2016). La, Ce, and Pr anomalies were $(La/La^*)_{SN} = La_{SN}/(Pr_{SN} \times (Pr_{SN}/Nd_{SN})^2)$, $(Ce/Ce^*)_{SN} = 2Ce_{SN}/(La_{SN} + Pr_{SN})$, and $(Pr/Pr^*)_{SN} = 2Pr_{SN}/(Ce_{SN} + Nd_{SN})$, respectively (the subscripted SN means PAAS-normalized) (Lawrence et al., 2006).

RESULTS

Petrography

Limestones of the Upper Member of the Yingshan Formation mainly comprise lime-mudstone, lime-wackstone, and lime-grainstone, with an average thickness of approximately 250 m. Lime-mudstones primarily composed of fine calcite crystals were generally deposited in a quiet hydrodynamic condition and are quite tight (**Figure 4A**). The intergranular pores between grains are occluded by drusy and blocky calcite cements in wackstones and grainstones (**Figures 4A,B**). Various types of bedding-parallel stylolites are present in micrite lime-mudstone (**Figures 4C,D**) or at lithological transitional interfaces between wackstones and mudstones (**Figure 4A**). The euhedral dolomites and blocky calcites appear in the vicinity of stylolites, suggesting intensive cementation (Wu et al., 2021). The optical petrographic analysis of core and thin section indicates that the primary intergranular pores developed during deposition were rarely preserved because of intensive compaction and cementation.

Reservoirs consist primarily of fractures (**Figure 4D**), microfractures, dissolved pores (**Figure 4C**), and paleocaves in Yingshan limestones of Tahe Oilfield. The paleocaves and fractures are the most significant hydrocarbon reservoirs in the study area, which demonstrate obvious blowdown and leakage phenomenon during the drilling process. According to the investigation of drilling process and imaging logging, the karst paleocave reservoirs have two major distribution modes, that is, either distributed in layers or developed along fractures (**Figure 3**).

Part of the paleocaves and fractures are partially or completely filled by calcites, which are the only cements in the study area. The CFC occurs as blocky crystals with a size larger than 1,000 μm and is characterized by dull red to red luminescence (**Figures 4F,G**). CFCs are encountered in the top of the caves in the Well TH12374CX (0.3 m thick) and TS3 (1.4 m thick) in the Yingshan limestones (**Figure 3**), and no mechanical fillings or breccia were observed. In addition, these fractures and associated paleocaves crosscut burial stylolites, suggesting that CFC postdates burial stylolites (**Figure 4D**).

Fluid Inclusion Studies

Fluid Inclusion Petrography

Aqueous inclusions are analyzed in CFC cements, with various sizes (3–50 μm) and irregular shapes. These aqueous inclusions occur as isolated or in trails crosscutting crystals (**Figures 5A,C**), which are interpreted as the secondary origin. Isolated fluid inclusions are separated from other inclusions by distances much larger than the size of the inclusions, whereas those in trails are relatively close to each other (**Figures 5A,B**). Two types of aqueous inclusions are distinguished by their phase assemblages and vapor/liquid ratios: (1) liquid-dominated biphase (liquid + vapor) aqueous inclusions, with vapor percentage <50% (L-D) (**Figures 5B,D**) and (2) liquid-only monophase aqueous inclusions (L-O) (**Figures 5B,D**). FIAs are distinguished as the most finely recognizable fluid inclusion entrapment events (Goldstein, 2001). The liquid-only and liquid-dominated fluid inclusions commonly coexist within individual trails, and they are considered to belong to the same FIA (**Figures 5B,D**).

Fluid Inclusion Microthermometry

Sixteen groups of FIAs are recognized for microthermometry in CFC. Homogenization temperature (T_h), ice-melting temperatures ($T_{m\text{-}ice}$), and metastable freezing temperatures (T_f) were measured on 92 L-D biphase inclusions. All the microthermometric data are demonstrated in **Table 1**, and the results are presented in histograms in **Figure 7**.

L-O aqueous inclusions were supercooled to −180°C to stretch and induce vapors, and some of them generated vapors once or several times during supercooling. The L-D biphase aqueous inclusions (including the L-O aqueous inclusions with vapor that appeared during supercooling) that coexisted with the L-O aqueous inclusions were tested for T_h values in six FIAs (n = 21). These inclusions exhibit inconsistent T_h values, spreading from 85°C to higher than 200°C (**Table 1**). The L-O aqueous inclusions were subsequently heated and stretched for $T_{m\text{-}ice}$ measurement. The overall range of T_f values in CFC cements is from −65°C to −40°C, with most values greater than −50°C. These aqueous inclusions have $T_{m\text{-}ice}$ values ranging from −6°C to 0°C (salinities of 0–9.4 wt% NaCl) with bimodal at −0.9°C and 0°C, respectively. Only seven inclusions in this type have $T_{m\text{-}ice}$ values below −1.9°C (**Table 1**; **Figure 7**).

Isotope Studies

Five MCs and 13 CFC samples from the Yingshan Formation in the coverage area were analyzed for carbon, oxygen, and strontium isotopic compositions (**Table 2**; **Figures 8**, **9**). The $\delta^{13}C$ values of the MCs have narrow ranges, typically varying from −1.0‰ to −0.4‰ (n = 5). In comparison, the $\delta^{18}O$ values spread from −8.6‰ to −6.4‰, with an average value of −7.5‰. For CFC, the $\delta^{13}C$ values (−2.3‰ to 0‰, n = 13) overlap with those of the MCs, whereas the $\delta^{18}O$ values (−15.3 to −12.5‰) are notably lower than those of MCs. The $^{87}Sr/^{86}Sr$ ratios of the MC samples range from 0.70880 to 0.70894, with an average 0.70888 ($n = 5$). CFCs have the $^{87}Sr/^{86}Sr$ ratios varying between 0.70955 and 0.70990, which are significantly higher than those of the MCs.

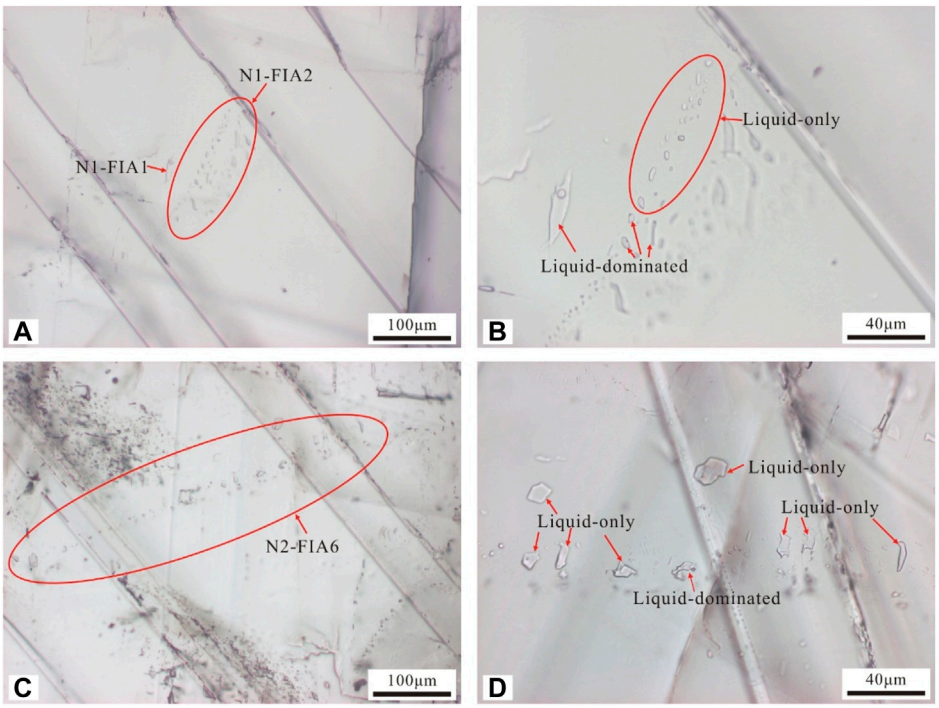

FIGURE 5 | The petrographic characteristics of fluid inclusions in CFC. **(A,B)** Liquid-dominated and liquid-only aqueous inclusions coexisting in trails N1, TS3, 6,100.32 m, $O_{1\text{-}2}y$. **(C,D)** Liquid-dominated and liquid-only aqueous inclusions coexisting in trails N2, TS3, 6,100.32 m, $O_{1\text{-}2}y$.

Trace Elements

The individual LA spot elemental values (n = 11) are summarized in **Table 3**, and their REEY patterns are illustrated in **Figure 6**. The total rare earth element (ΣREE) contents of CFC samples vary between 0.65 and 1.60 ppm (mean 0.95 ± 0.30 ppm) (**Table 3**). The REEY distributions exhibit (1) positive La (1.71–3.42, 2.63 ± 0.61) and Y (2.09–2.48, 2.29 ± 0.14) anomalies, and negative Ce (0.58–0.75, 0.63 ± 0.49) anomalies, (2) superchondritic Y/Ho ratios (55.27–68.92, 60.30 ± 3.73), (3) LREE depletion relative to HREE (Pr/Yb = 0.63 ± 0.15), and (4) MREE enrichment (BSI values of 1.24–1.68, 1.40 ± 0.12).

CFC samples have moderate Sr, Mn, and Fe concentrations of 115.48–263.51, 126.42–176.09, and 386.16–428.60 ppm, respectively (**Table 3**). The calculated Mn/Sr ratios spread from 0.48 to 1.47 with an average value of 0.76 ± 0.36 (**Table 3**). All the CFC samples have low Al and Zr concentrations, with Al contents of 0.017–0.318 ppm (n = 9) and Zr contents of 0.011–0.030 ppm (n = 11) (**Table 3**). The samples exhibit poor correlations among REE, Al, and Zr contents (**Figure 10A**).

DISCUSSION

Interpretation of Fluid Inclusion and Geochemical Data

Fluid Inclusion Data

In order to decipher the origin of the diagenetic fluids by aqueous fluid inclusion data, the aqueous inclusion petrography is emphasized here. These measured secondary aqueous inclusions in trails comprise L-O monophase and L-D biphase inclusions (**Figure 5**). Vapors of the L-O inclusions rarely appear during supercooling, and the coexisted L-D inclusions have inconsistent T_h values (**Table 1**). The T_f and $T_{m\text{-}ice}$ values of both types of the inclusions mainly distribute in −45°C to 40°C and −1.4°C to 0°C, respectively, suggesting that they have extremely low salinities (Steele-MacInnis et al., 2011; Wilkinson, 2017). Overall, the fluid inclusions in CFC are characterized by inconsistent T_h and low salinities. The findings imply that the L-O aqueous inclusions were trapped in the low-temperature environment (<50°C), and the coexisted L-D inclusions resulted from re-equilibration during burial diagenesis (Goldstein and Reynolds, 1994).

The meteoric water usually has a low salinity with the $T_{m\text{-}ice}$ values close to 0°C in fluid inclusions (Goldstein and Reynolds, 1994; Wilkinson, 2017). The $T_{m\text{-}ice}$ values of −1.4°C to 0°C are higher than modern seawater (−1.9°C) (**Figure 7A**), indicating that aqueous fluid may trap the paleo-meteoric water. Obviously, the fluid inclusions in CFC are divided into two groups on the $T_{m\text{-}ice}$ histogram, with one group having higher $T_{m\text{-}ice}$ of −0.4°C to 0°C (the highest $T_{m\text{-}ice}$ value is 0°C in individual FIA) (**Figure 7B**) and the other having relatively lower $T_{m\text{-}ice}$ of −1.4 to 0.7°C (the highest $T_{m\text{-}ice}$ value is −0.7°C in individual FIA) (**Figure 7C**). These high-salinity inclusions may trap paleo-meteoric waters, which experienced re-equilibration or slightly mixing between freshwater and porewater (Goldstein and Reynolds, 1994; Li et al., 2017).

TABLE 1 | Fluid inclusion microthermometric data.

Trails	FIA	Well name	Depth (m)	Host mineral	N	Size (μm)	Inclusion types[a]	Homogenization temperatures (°C) (N)	Metastable freezing temperatures (°C)	Ice final melting temperatures (°C) (N)	Salinities (wt%)
N1	FIA1	TS3	6,100.52	CFC	1	50	L-D	150 (1)	−40	0 (1)	0
	FIA2			CFC	8	6–40	L-O		−50 to 40	−6 to 0 (8)	0–9.4
	FIA3			CFC	5	6–42	L-O, L-D	110 to >200 (2)	−40	0 (3)	0
	FIA4			CFC	10	3–24	L-O, L-D	120 to >200 (7)	−40	0 (3)	0
	FIA5			CFC	11	5–44	L-O		−45 to 40	−0.1 (11)	0
	FIA6			CFC	8	4–14	L-O		−45 to 40	−1.2 to 0 (8)	0—1.9
N3	FIA1			CFC	9	6–45	L-O, L-D	85–145 (5)	−65 to 40	−6 to 0 (9)	0–9.4
	FIA2			CFC	7	4–8	L-O, L-D		−40	0 (7)	0
	FIA3			CFC	3	4–9	L-O, L-D		−40	−0.1 to 0 (3)	0
N2	FIA1			CFC	13	3–13	L-O, L-D	125 (1)	−45 to 40	−0.9 to 0.7 (13)	1.0–1.4
	FIA2			CFC	6	4–18	L-O		−40	−0.8 to 0.7 (6)	1.0–1.2
	FIA3			CFC	7	5–30	L-O, L-D	>200 (2)	−45 to 40	−2.5 to 0.7 (6)	1.0–4.2
	FIA4			CFC	2	12–18	L-O, L-D		−50 to 45	−4.1 to 0.8 (2)	1.2–6.8
	FIA5			CFC	1	16	L-D		−50	−4.2 (1)	6.9
	FIA6			CFC	6	7–19	L-O		−45 to 40	−1 to 0.8 (6)	1.2–1.6
	FIA7			CFC	5	4–16	L-O		−45 to 40	−0.9 (5)	1.4

[a]*L-O, liquid-only monophase aqueous inclusions; L-D, liquid-dominated biphase aqueous inclusions.*

TABLE 2 | The isotopic compositions of micrite limestone and CFC in the coverage area.

Well No	Formation	Depth (m)	Lithology	$\delta^{13}C$ (‰, VPDB)	$\delta^{18}O$ (‰, VPDB)	$^{87}Sr/^{86}Sr$ error(δ)
TS301	$O_{1\text{-}2}y$	6,130.35	MC	−0.8	−7.1	0.70889 (4×10^{-6})
TS301	$O_{1\text{-}2}y$	6,206.00	MC	−0.8	−6.4	0.70880 (3×10^{-6})
TS3	$O_{1\text{-}2}y$	6,107.80	MC	−0.4	−8.6	0.70894 (4×10^{-6})
TS3	$O_{1\text{-}2}y$	6,112.20	MC	−1.0	−8.1	0.70891 (5×10^{-6})
TS3	$O_{1\text{-}2}y$	6,112.70	MC	−1.0	−7.5	0.70885 (4×10^{-6})
TS3	$O_{1\text{-}2}y$	6,100.00	CFC	−1.3	−14.1	0.70966 (4×10^{-6})
TS3	$O_{1\text{-}2}y$	6,100.32	CFC	−1.9	−13.0	0.70960 (3×10^{-6})
TS3	$O_{1\text{-}2}y$	6,100.37	CFC	−2.3	−13.7	0.70955 (3×10^{-6})
TS3	$O_{1\text{-}2}y$	6,100.52	CFC	−2.3	−13.6	0.70956 (3×10^{-6})
TS3	$O_{1\text{-}2}y$	6,100.56	CFC	−2.0	−14.1	0.70963 (3×10^{-6})
TS3	$O_{1\text{-}2}y$	6,106.00	CFC	−1.2	−15.0	0.70971 (4×10^{-6})
TS3	$O_{1\text{-}2}y$	6,106.25	CFC	−1.3	−13.5	0.70967 (4×10^{-6})
TS3	$O_{1\text{-}2}y$	6,106.30	CFC	−1.6	−13.2	0.70970 (3×10^{-6})
TS3	$O_{1\text{-}2}y$	6,106.81	CFC	−1.7	−15.3	0.70970 (4×10^{-6})
TH12374CX	$O_{1\text{-}2}y$	6,284.63	CFC	−1.2	−14.0	0.70982 (3×10^{-6})
TH12374CX	$O_{1\text{-}2}y$	6,284.70	CFC	−1.8	−14.6	0.70990 (4×10^{-6})
TH12374CX	$O_{1\text{-}2}y$	6,287.20	CFC	−0.8	−12.7	0.70986 (3×10^{-6})
TH12374CX	$O_{1\text{-}2}y$	6,287.27	CFC	0.0	−12.5	0.70985 (3×10^{-6})

TABLE 3 | *In situ* rare earth elements and yttrium (REEY) concentrations (in ppm) of CFC samples and modern Bahama ooids (from Li et al., 2019).

Sample ID	CFC-1	CFC-2	CFC-3	CFC-4	CFC-5	CFC-6	CFC-7	CFC-8	CFC-9	CFC-10	CFC-11	Modern Bahama ooids[a]
Well	TS3	TS3	TS3	TS3	TS3	TS3	TS3	TS3	TS3	TS3	TS3	
Depth (m)						6,100.52						
Al	0.228	0.318	0.209	0.210	0.208	0.216	0.301	0.017		0.166		
Mn	128.06	130.66	126.42	131.19	128.58	132.64	134.22	170.22	176.09	156.73	151.46	
Fe	418.69	428.36	428.6	427.81	427.46	408.00	407.25	386.46	397.17	396.74	386.16	
Sr	261.68	262.52	260.91	263.51	253.41	223.28	209.95	115.48	122.93	141.98	231.94	
Zr	0.022	0.018	0.018	0.020	0.013	0.030	0.023	0.025	0.019	0.014	0.011	
La	0.238	0.237	0.269	0.226	0.231	0.301	0.277	0.294	0.340	0.427	0.320	0.159
Ce	0.210	0.200	0.223	0.184	0.203	0.264	0.246	0.320	0.366	0.498	0.375	0.185
Pr	0.019	0.020	0.023	0.017	0.022	0.027	0.025	0.040	0.045	0.062	0.037	0.041
Nd	0.077	0.076	0.078	0.063	0.070	0.118	0.109	0.170	0.196	0.264	0.187	0.205
Sm	0.017	0.016	0.019	0.016	0.015	0.020	0.022	0.035	0.039	0.055	0.038	0.063
Eu	0.006	0.004	0.005	0.003	0.005	0.006	0.006	0.009	0.012	0.012	0.009	0.019
Gd	0.039	0.038	0.044	0.034	0.037	0.046	0.049	0.080	0.094	0.091	0.077	0.11
Tb	0.005	0.006	0.007	0.006	0.007	0.007	0.007	0.010	0.010	0.012	0.008	0.018
Dy	0.053	0.048	0.048	0.043	0.049	0.055	0.049	0.074	0.091	0.080	0.082	0.129
Y	0.687	0.593	0.743	0.640	0.677	0.727	0.719	1.081	1.137	0.992	1.150	1.607
Ho	0.011	0.010	0.012	0.010	0.011	0.012	0.012	0.018	0.021	0.018	0.017	0.033
Er	0.030	0.029	0.029	0.029	0.027	0.032	0.032	0.049	0.052	0.050	0.045	0.102
Tm	0.003	0.002	0.003	0.003	0.004	0.004	0.003	0.005	0.006	0.005	0.004	0.013
Yb	0.014	0.012	0.014	0.011	0.010	0.013	0.009	0.022	0.024	0.020	0.020	0.074
Lu	0.001	0.002	0.001	0.002	0.001	0.001	0.001	0.003	0.004	0.003	0.001	0.011
REE	0.724	0.701	0.776	0.648	0.691	0.907	0.847	1.130	1.299	1.596	1.218	1.162
REE + Y	1.411	1.294	1.519	1.287	1.369	1.634	1.565	2.211	2.436	2.589	2.369	2.769
BSI	1.366	1.375	1.321	1.249	1.290	1.302	1.411	1.442	1.508	1.476	1.678	1.173
Y/Ho	61.34	56.95	62.06	61.12	63.65	59.83	59.55	59.25	55.35	55.35	68.92	48.70
$(La/La^a)_{SN}$	3.249	2.660	2.097	2.717	1.706	3.342	3.379	2.162	2.239	1.954	3.420	1.516
$(Ce/Ce^a)_{SN}$	0.628	0.595	0.581	0.588	0.601	0.608	0.615	0.661	0.658	0.689	0.749	0.528
$(Pr/Pr^a)_{SN}$	0.876	0.954	1.023	0.940	1.069	0.898	0.891	0.990	0.982	0.999	0.822	1.109
$(Pr/Yb)_{SN}$	0.436	0.552	0.523	0.508	0.668	0.645	0.866	0.566	0.607	0.985	0.601	0.177

[a]*From Li et al. (2019).*

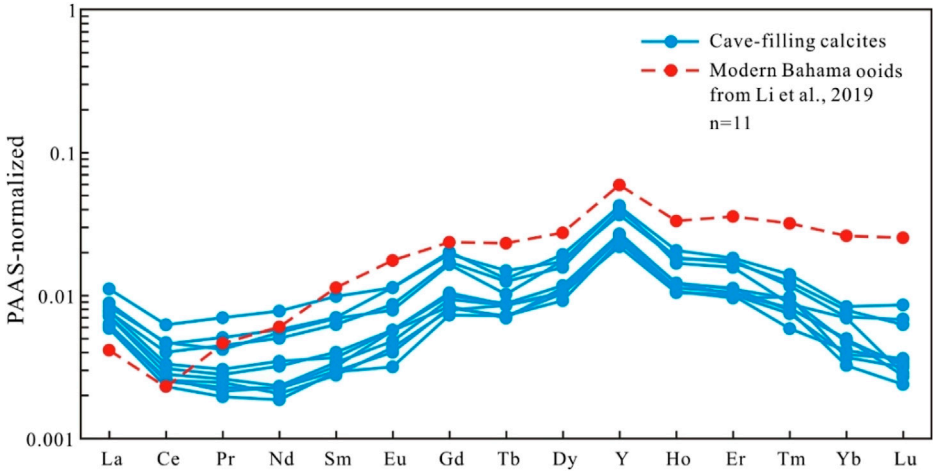

FIGURE 6 | PAAS-normalized REEY patterns of CFC and modern Bahama ooids (from Li et al., 2019).

Carbon, Oxygen, and Strontium Isotopic Compositions

Most of the MC samples obtained from the Yingshan Formation exhibit that the $\delta^{13}C$ and $\delta^{18}O$ values are within the respective $\delta^{13}C$ (−3‰ to +0.5‰) and $\delta^{18}O$ (−10‰ to −6‰) of Early-Middle Ordovician seawater summarized by Veizer et al. (1999). Two samples, however, have lower carbon and oxygen isotopic values (**Figure 8**). The $\delta^{13}C$ and $\delta^{18}O$ values of MC samples are positively correlated ($R^2 = 0.62$), indicating that recrystallization occurs in limestones in a closed system, and the porewater revised from seawater dominated in the system (Talbot, 1990; Machel et al., 1996; Arp et al., 2008).

Each $\delta^{18}O$ value of the CFC is particularly lighter compared with the Ordovician marine calcites in the coverage area. On the basis, together with the viewpoint of oxygen isotope fractionation by O'Neil et al. (1969), CFC with light $\delta^{18}O$ value may have been precipitated either from meteoric water or hydrothermal fluid with relatively high temperature.

The $^{87}Sr/^{86}Sr$ ratios of calcites are generally interpreted to closely reflect the strontium compositions of the fluids from what they precipitated. The $^{87}Sr/^{86}Sr$ ratios of the MC samples are completely within the $^{87}Sr/^{86}Sr$ ranges (0.7085–0.7090) of Early-Middle Ordovician marine calcites summarized by Veizer et al. (1999) (**Figure 9**). In addition, all the CFC samples demonstrate particularly higher $^{87}Sr/^{86}Sr$ ratios and Sr concentrations compared with the matrix limestone (**Figure 9** and **Table 3**). These infer that the diagenetic fluid may have obtained more radioactive Sr by interacting with ^{87}Sr-rich minerals or detrital rocks.

Consequently, carbon, oxygen, and strontium isotopic compositions of CFC indicate that the parent fluids may be freshwater or hydrothermal fluids. Because the fluid inclusion–trapped freshwaters are of secondary origin and the primary inclusions are masked by secondary ones, it is difficult to differentiate freshwaters and hydrothermal fluids based on C-O-Sr isotopic compositions and fluid inclusions.

Trace Elements

The carbonate minerals with low REE concentration are easily contaminated by siliciclastic materials with much higher REE concentrations (Li et al., 2019). Therefore, concentrations of screening elements, such as Al and Zr, were measured to screen possible contaminants in this study. The finding demonstrates that CFC has low Al (mean = 0.209 ± 0.086 ppm) and Zr concentrations (mean 0.020 ± 0.006 ppm). Also, there is noncorrelation among Al, Zr, and ΣREE concentrations (**Table 3** and **Figure 10A**). For these characteristics, CFC is believed to have negligible contamination by siliciclastic material.

The REEY patterns are characterized by LREE depletion relative to HREE, MREE enrichment, high Y/Ho ratios, negative Ce anomaly, and positive La and Y anomalies. MREE enrichment (BSI values >1), Ce enrichment ($(Ce/Ce^*)_{SN}$ ratios approaching 1), and higher Mn/Sr ratios generally resulted from recrystallization during burial diagenesis (Shields and Stille, 2001). The ΣREE is positively correlated to BSI, $(Ce/Ce^*)_{SN}$ and Mn/Sr ($R^2 = 0.52$, 0.63, and 0.56, respectively); that is, the more MREE enrichment, Ce enrichment, and higher Mn/Sr ratios, the higher REE concentrations (**Figure 10B**). Therefore, CFC calcites may have extremely low REE concentrations (<0.65 ppm), and the recrystallization during subsequently buried diagenesis makes the REE concentrations of CFC higher. The $(Ce/Ce^*)_{SN}$ ratios range from 0.58 to 0.75 (0.63 ± 0.05), and the $(Pr/Pr^*)_{SN}$ ratios are 0.82–1.07 (0.95 ± 0.07) (**Figure 10C**), suggesting that the CFC samples display an analytically significant positive La anomaly (Bau and Alexander., 2009). The positive correlation between $(Ce/Ce^*)_{SN}$ ratios and BSI ($R^2 = 0.87$) signifies that the decreased negative Ce anomalies may be due to recrystallization during burial diagenesis (**Figure 10D**).

Moreover, the overall REEY patterns of CFC are similar to the seawater-like proxies, but there still exists differentiation between them. The similarity suggests that the CFC may be inherited from

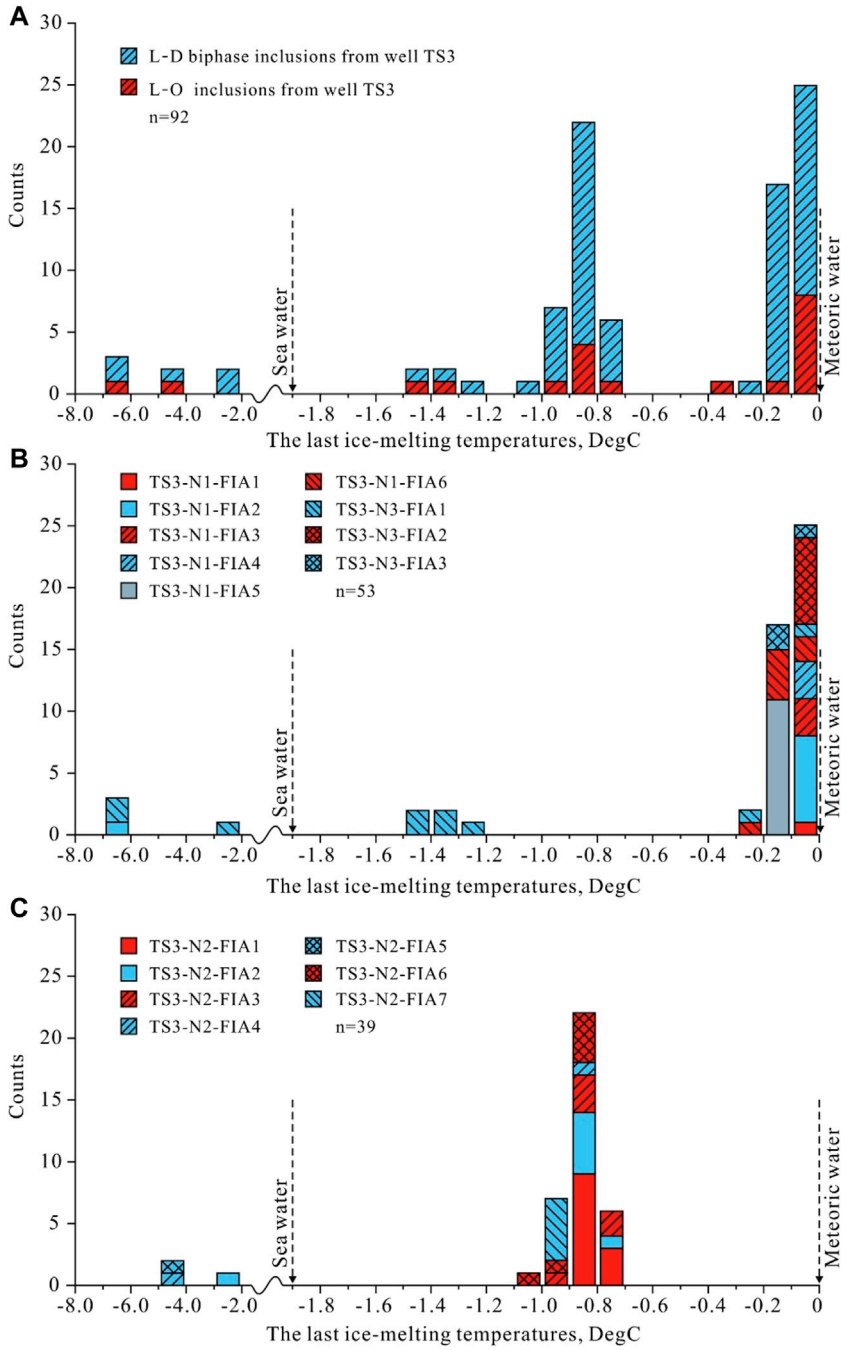

FIGURE 7 | (A) Histograms of ice-melting temperatures of fluid inclusions in TS3. **(B)** Histograms of $T_{m\text{-}ice}$ with the highest $T_{m\text{-}ice}$ of 0°C in individual FIA. **(C)** Histograms of $T_{m\text{-}ice}$ with the highest $T_{m\text{-}ice}$ of –0.7°C in individual FIA. The petrographic evidence that supports the FIAs can be found in **Figure 5**; **Table 1**.

seawater. In addition, REE elements can be largely retained during meteoric diagenesis, with precipitating cements taking up excess REE elements released from dissolved carbonate (Webb et al., 2009). However, depletion in HREE may reflect the removal of HREE by mineral breakdown, alteration, and precipitation during fluid–rock interaction. The REEY results indicate that the CFC may be seawater origin or precipitate from dissolved host carbonate during meteoric diagenesis, but significantly altered by recrystallization. Bau et al. (2003) have argued that the REEY in the diagenetic fluid may be derived from the local country rock.

The Fluids Nature and Origin of Cave-Filling Calcites

Because the low-temperature (<50°C) meteoric fluid inclusions are of secondary origin, two scenarios are assumed here: (1) the CFCs are not precipitated from freshwater but are leached by it; (2) the CFCs are precipitated from freshwater and the freshwater

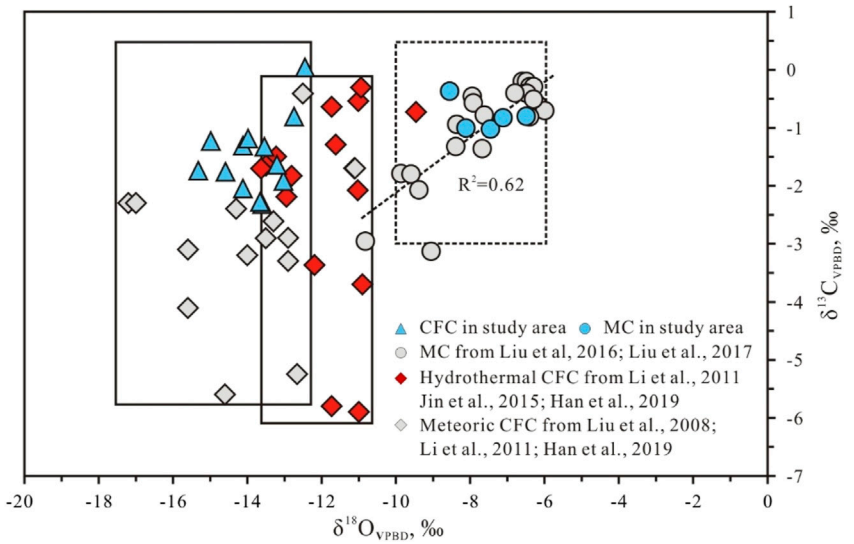

FIGURE 8 | A scatter diagram of $\delta^{18}O$ and $\delta^{13}C$ in the Yingshan Formation. The dashed box presents the isotopic value range of Early-Middle Ordovician marine calcite summarized by Veizer et al. (1999). The solid-line areas indicate the isotopic value ranges of various CFCs.

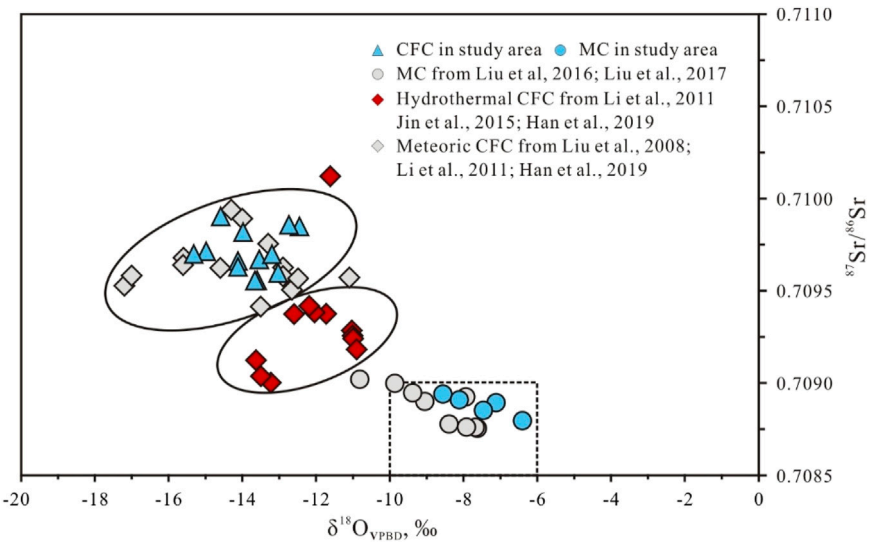

FIGURE 9 | A scatter diagram of $\delta^{18}O$ values and $^{87}Sr/^{86}Sr$ ratios in the Yingshan Formation. The dashed box signifies the isotopic value range of marine calcites summarized by Veizer et al. (1999). The solid-line areas indicate the isotopic value ranges of various CFCs.

are trapped in both primary inclusions, which are not identified by the fluid inclusion petrography and subsequent secondary inclusions. Here, we proposed that the second scenario may be true, and the reasons are as follows.

First, the secondary inclusions suggest that CFC experienced a low-temperature environment, and the oldest time that the samples (the burial depth of 6,100 m in the Well TS3) reached 50°C is approximately the Early Carboniferous, depending on the 1-D burial-thermal history of Well TS3 (**Figure 11**, Liu et al., 2017). Furthermore, the highest temperature the CFC underwent before the Early Carboniferous is approximately 75°C, and the lowest one is the surface temperature of 20°C. Oxygen isotopic fractionation occurred between calcite and fluid during the precipitation. The parent fluids $\delta^{18}O_{water}$ (SMOW) values are calculated by the O'Neil et al. (1969) oxygen fractionation equation. With the temperature range (20°C–75°C) and the measured $\delta^{18}O$ values of the CFC samples, the calculated $\delta^{18}O_{water}$ values of the parent fluids range from −14.4‰ to 2.2‰ (**Figure 12**). The range of the parent fluids $\delta^{18}O_{water}$ values and the REEY patterns of CFC both suggest that the

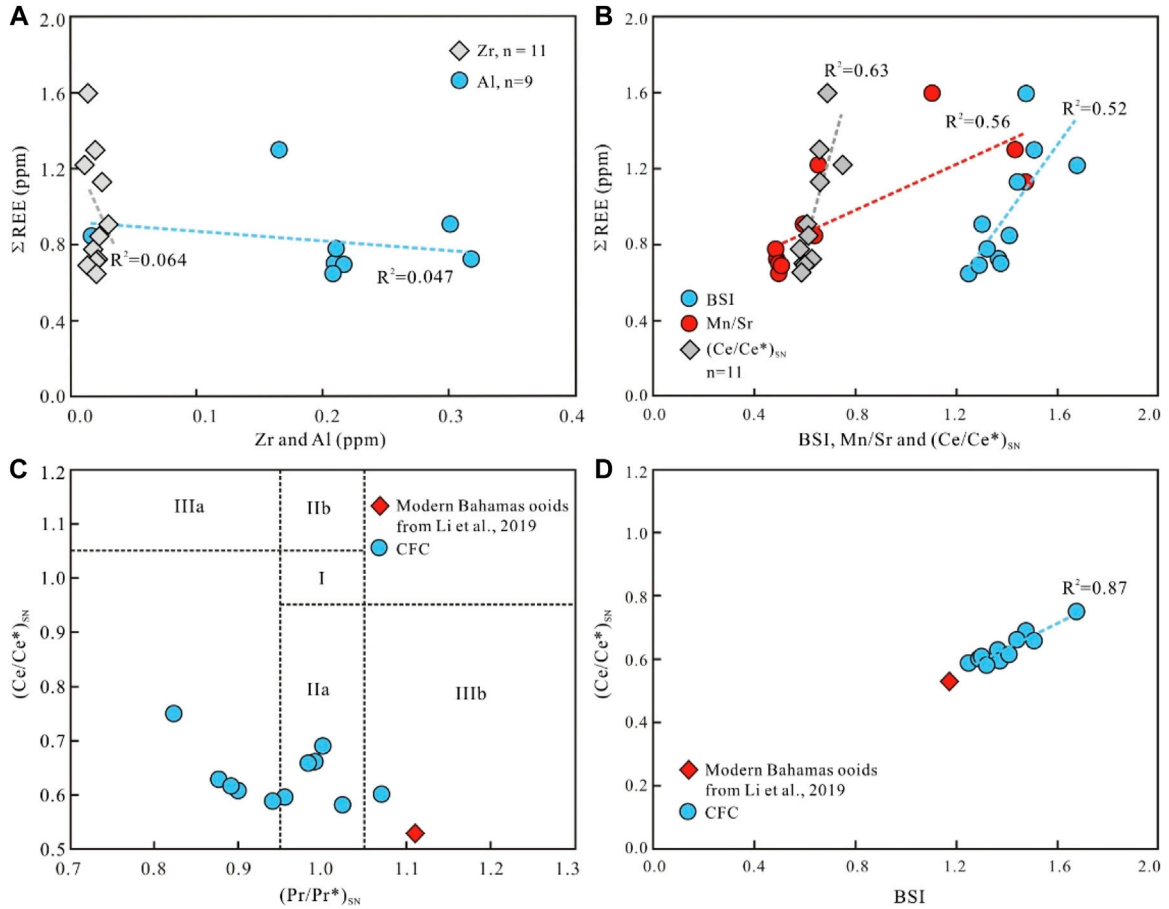

FIGURE10 | (A) Plots of Al and Zr content versus total REE concentration in the studied CFC samples. **(B)** Cross plot among ΣREE and BSI, Mn/Sr, and Ce anomaly, showing all positive correlation. **(C)** Diagram discriminating between La and Ce anomalies (after Bau and Alexander, 2009). The CFC samples are characterized by a significant positive La anomaly. **(D)** Cross plot between BSI values (MREE enrichment) and Ce anomalies showing strong positive correlation.

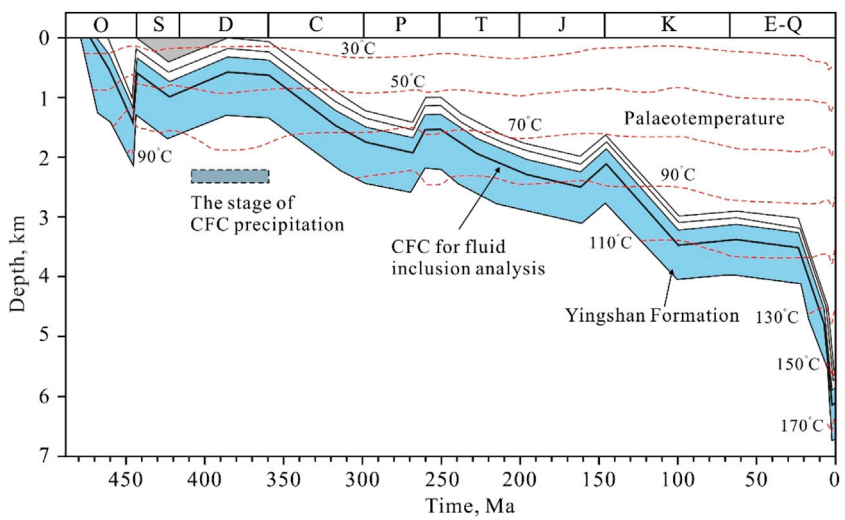

FIGURE 11 | The 1-D burial-thermal history of Well TS3 (from Liu et al., 2017). The blue band represents the Lower–Middle Yingshan Formation. The gray band indicates the Silurian successions.

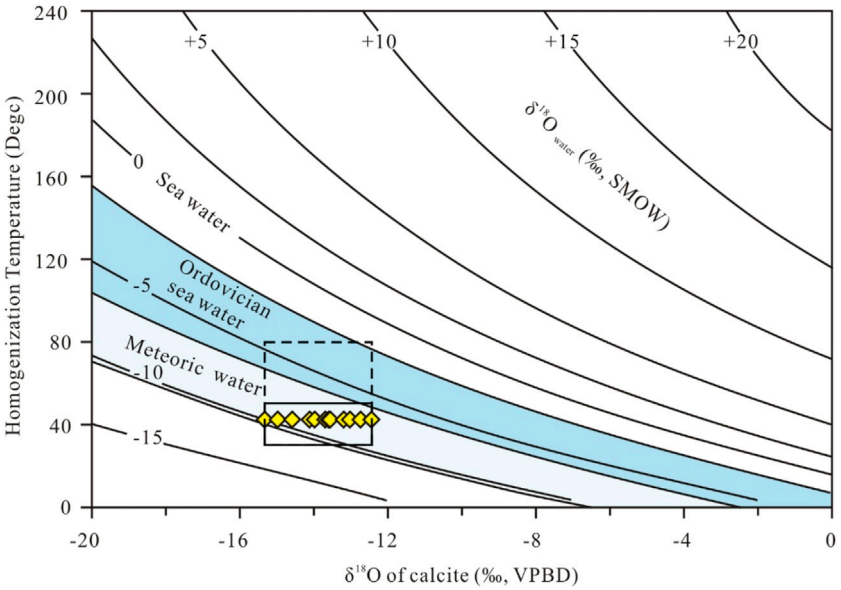

FIGURE 12 | Temperature versus $\delta^{18}O$ diagenetic fluid for $\delta^{18}O$ values of CFC using the calcite-water equation (10)^{3}ln$\alpha_{calcite\text{-}water}$ = 2.78 × 10^6 T^{-2} − 2.89 (O'Neil et al., 1969). Solid box represents that the parent fluids is meteoric water with $\delta^{18}O_{water}$ values (−13.8 to 5.8) when the temperature is 30°C–50°C.Dashed box indicates that the parent fluid is Ordovician seawater with $\delta^{18}O_{water}$ values (−5.8 to 2.2) when the temperature is 50°C–75°C.

diagenetic fluids may be derived from freshwater or Ordovician seawater. However, the Sr isotopic compositions of the calcites are more radioactive than those of the Ordovician seawater (**Figure 8** and **Figure 9**). Therefore, the hypothesis that calcites are precipitated from seawater or porewater that are modified from seawater is excluded.

Second, the REEY patterns of CFC are different from those of the hydrothermal dolomite and calcites (Zhu et al., 2013; Jin et al., 2015; Zhang et al., 2015; Liu et al., 2020). In addition, the CFC has comparatively higher $^{87}Sr/^{86}Sr$ ratios and lower $\delta^{18}O$ values in the study area than those of hydrothermal calcites (**Figure 8** and **Figure 9**). Furthermore, any other accompanied hydrothermal minerals are not observed in the study area. These evidences indicate that CFC is unlikely precipitated from hydrothermal fluids.

The REEY compositions are largely controlled by fluid–mineral equilibria when meteoric fluids interact with host rocks because meteoric fluids are virtually devoid of REEY (Debruyne et al., 2016). Thus, CFC can exhibit seawater-like REEY patterns and low ΣREE concentrations (<0.65 ppm), when meteoric water leached marine carbonate (Johannesson et al., 2006; Bourdin et al., 2011), whereas the high $^{87}Sr/^{86}Sr$ ratios suggest the fluid leached the overlying sandstone. Bau et al. (2003) observed this characteristic in fluorite from MVT deposits in the Pennine Orefield, England, and suggested that the trace metal irons released from bulk aluminosilicate rocks are incongruent during fluid–rock interaction and fluid migration. Consequently, we propose that the CFC may be precipitated from freshwater that leached the host limestones.

As a quintessential meteoric calcite, CFC was supposed to be precipitated either in the late Middle Ordovician or Devonian periods. It seems unlikely that the origin of CFC could be related to the Late Middle Ordovician event, because the burial depth was less than 600–700 m (Lu et al., 2017), which was insufficient to generate high-amplitude stylolites crosscut by CFC. Zhang et al. (2005) measured the $^{87}Sr/^{86}Sr$ ratios of calcites formed during the late Middle Ordovician, which are lower than 0.70940, and corroborated this point simultaneously. In comparison, the $^{87}Sr/^{86}Sr$ ratios of CFC precipitated in the Devonian period exceeded 0.70940 (Zhang et al., 2005; Li et al., 2011). Therefore, we inferred that the lighter $\delta^{18}O$ and more radiogenic $^{87}Sr/^{86}Sr$ signatures may be mixing of exotic radiogenic ^{87}Sr with the detrital rocks. The possible explanation is that Silurian siliciclastic sediments above the Ordovician strata are the likely source for the high radiogenic ^{87}Sr in the migrating meteoric water. Besides, pore fluids having interacted with the Silurian sandstones containing feldspathic components could mix with descending meteoric water. On this basis, these CFCs could be ascribed to the meteoric water origin in Early Hercynian karstification during the Devonian period.

Model of Karstification in Nonexposed Limestones

According to the above context, the Early Hercynian karstification is responsible for the CFC and well-developed paleocave reservoirs in the coverage area. However, it is worth mentioning that the Yingshan limestone is overlain by the Middle to Upper Ordovician insoluble strata during the Early Hercynian stage, so the limestone cannot be leached directly by freshwater flowing down (Yang et al., 2014). Therefore, based on the geochemical characteristics of CFC samples and paleocave distribution, two possible karst models are as follows: (1) the freshwater flowed down into the Yingshan limestone along with the fracture systems; and (2) the meteoric water migrated laterally along the permeable strata from the buried-hill area.

On the one hand, a large number of strike-slip, tensile, and reverse faults have been formed during the uplift according to

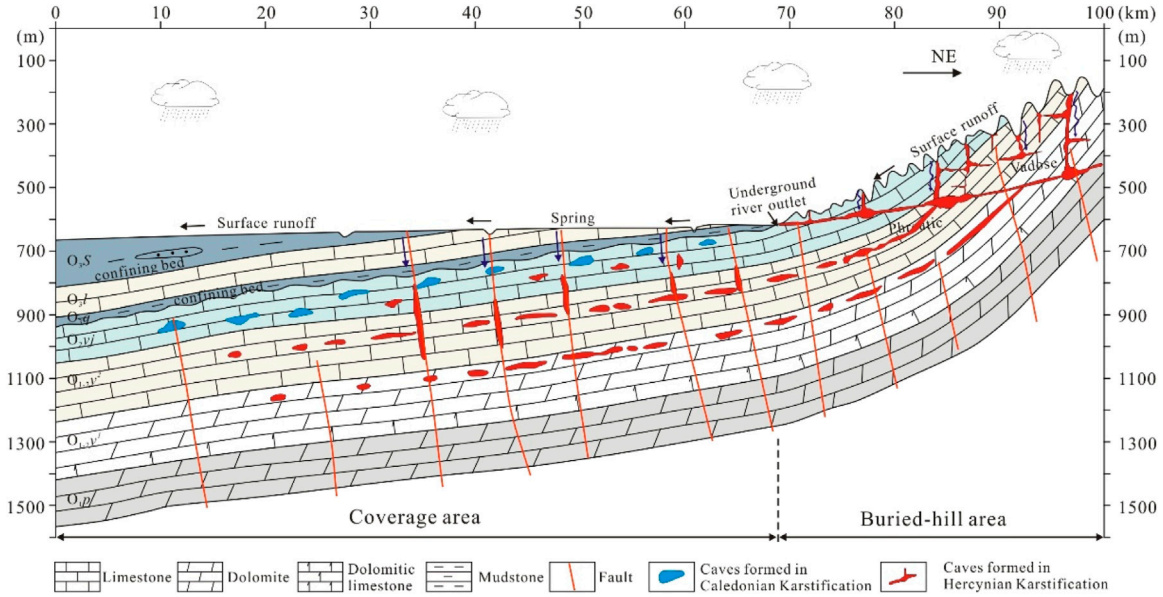

FIGURE 13 | Meteoric water karstification model in nonexposed limestone of Tahe area.

previous studies (Lu et al., 2017; Méndez et al., 2019). The faults penetrating insoluble strata provide the main karstification pathways for the initial karstic reservoirs development. In general, meteoric water would infiltrate the Yingshan limestones along the fractures leading directly to the surface under gravity, and the dissolved pores and caves developed ultimately (**Figure 13**). In addition, the faults and related-karstic reservoirs can also be the hydrocarbon migration passageways and the accumulation traps.

On the other hand, meteoric water can laterally migrate along the highly permeable strata to coverage area from buried-hill area under the paleogeomorphic height difference (Qi and Yun, 2010; Dan et al., 2015). The substratified distribution of paleocaves also supports the possibility of lateral migration of meteoric water. Besides, the farther away from the Upper Ordovician pinch-out boundary, the deeper the paleocaves (**Figure 3**), which also indicates that the meteoric water may be migrated from the buried-hill area. The dissolved pores and caves develop along the meteoric water lateral migration. During the charging of meteoric water, calcites precipitated in the dissolved pores and caves from the fluid saturated with calcium carbonate. Therefore, calcites precipitated from meteoric water accompanied with depleted $\delta^{18}O$, high $^{87}Sr/^{86}Sr$ ratios, low ΣREE, and low homogenization temperature of fluid inclusion.

CONCLUSION

1) Detailed petrographic studies of the Yingshan fracture-paleocave carbonate rocks in the Tahe Oilfield reveal that the paleocaves are either layered distribution or developed along fractures. Paleocaves and fractures are filled only with blocky calcite cements (CFC), which crosscut the burial stylolites.
2) By systematic fluid inclusion observation, liquid-only monophase and aqueous inclusions and liquid-dominated aqueous inclusions with low salinities in trails are recognized, indicating the CFC has experienced low-temperature environment (<50°C). The low $\delta^{18}O$ values, seawater-like REEY patterns, and low ΣREE (<0.65 ppm) have recorded that the CFCs are meteoric water origin that leached the Yingshan limestone. The relatively higher $^{87}Sr/^{86}Sr$ ratios were attributed to the meteoric water interacting with the overlying Silurian detrital rock during percolating downward. The meteoric water generated during the Early Hercynian karstification event is responsible for the CFC formation.
3) For Yingshan nonexposed limestone, meteoric water karstification generated by flowing downward along the fractures penetrating insoluble strata and/or migrating laterally along the permeable strata though the overlying thick insoluble strata in the coverage area.

DATA AVAILABILITY STATEMENT

The original contributions presented in the study are included in the article/Supplementary Material, further inquiries can be directed to the corresponding authors.

AUTHOR CONTRIBUTIONS

YZ: Conceptualization, Methodology, Writing-Original Draft, Formal analysis SZ: Supervision, Writing-Review Editing BH: Supervision, Writing-Review Editing ZL: Visualization, Data Curation, Project administration NY: Investigation BZ: Project administration XH: Software FX: Software XB: Investigation XZ: Software.

FUNDING

This research was supported by the financial support from the National Natural Science Foundation of China (No. 42102191 and 41902239).

ACKNOWLEDGMENTS

Special thanks go to Dr. Xiucheng Tan and Dr. Dongfang Zhao of the Laboratory of Carbonate Sedimentary and Diagenetic Geochemistry for collection and analyses of the *in-situ* trace elemental data.

REFERENCES

Ainsaar, L., Kaljo, D., and Martma, T. (2010). Middle and Upper Ordovician Carbon Isotope Chemostratigraphy in Baltoscandia: A Correlation Standard and Clues to Environmental History. *Palaeogeogr. Palaeoclimatol. Palaeoecol.* 294 (3), 189–201. doi:10.1016/j.palaeo.2010.01.003

Arp, G., Ostertag-Henning, C., Yücekent, S., Reitner, J., and Thiel, V. (2008). Methane-Related Microbial Gypsum Calcitization in Stromatolites of a marine Evaporative Setting (Münder Formation, Upper Jurassic, Hils Syncline, North Germany). *Sedimentology* 55 (5), 1227–1251. doi:10.1111/j.1365-3091.2007.00944.x

Bau, M., and Alexander, B. W. (2009). Distribution of High Field Strength Elements (Y, Zr, REE, Hf, Ta, Th, U) in Adjacent Magnetite and Chert Bands and in Reference Standards FeR-3 and FeR-4 from the Temagami Iron-Formation, Canada, and the Redox Level of the Neoarchean Ocean. *Precambrian Res.* 174, 337–346. doi:10.1016/j.precamres.2009.08.007

Bau, M., Romer, R. L., Lüders, V., and Dulski, P. (2003). Tracing Element Sources of Hydrothermal Mineral Deposits: REE and Y Distribution and Sr-Nd-Pb Isotopes in Fluorite from MVT Deposits in the Pennine Orefield, England. *Miner Deposita* 38, 992–1008. doi:10.1007/s00126-003-0376-x

Bourdin, C., Douville, E., and Genty, D. (2011). Alkaline-Earth Metal and Rare-Earth Element Incorporation Control by Ionic Radius and Growth Rate on a Stalagmite from the Chauvet Cave, Southeastern France. *Chem. Geology.* 290, 1–11. doi:10.1016/j.chemgeo.2011.08.006

Chen, Q., Zhao, Y., Li, G., Chu, C., and Wang, B. (2012). Features and Controlling Factors of Epigenic Karstification of the Ordovician Carbonates in Akekule Arch, Tarim Basin. *J. Earth Sci.* 23 (4), 506–515. doi:10.1007/s12583-012-0271-4

Dan, Y., Liang, B., Zhang, Q. Y., Cao, J. W., Li, J. R., and Hao, Y. Z. (2015). Characteristic and Genesis of Ordovician Carbonate Karst Reservoir in the Shallow Coverage Zone of Halahatang Area, Northern Tarim Basin. *Geophys. Prospecting Pet.* 54 (1), 90–98. doi:10.3969/j.issn.1000-1441.2015.01.013

Debruyne, D., Hulsbosch, N., and Muchez, P. (2016). Unraveling Rare Earth Element Signatures in Hydrothermal Carbonate Minerals Using a Source-Sink System. *Ore Geology. Rev.* 72, 232–252. doi:10.1016/j.oregeorev.2015.07.022

Feng, Z. Z., Bao, Z. D., Wu, M. B., Jin, Z. K., Shi, X. Z., and Luo, A. R. (2007). Lithofacies Palaeogeography of the Ordovician in Tarim Basin. *J. Palaeogeogr.* 9 (5), 447–460. doi:10.3969/j.issn.1671-1505.2007.05.003

Fu, J. H., Bai, H. F., and Sun, L. Y. (2012). Types and Characteristics of the Ordovician Carbonate Reservoirs in Ordos Basin. *Acta Petrolei Sinica* 34 (S2), 110–117. doi:10.7623/syxb2012S2010

Gao, L. J., Li, Z. J., Li, H. Y., and Huang, C. (2020). Classification and Characteristic Analysis of Super-Deep Carbonate Reservoirs in Tarim Basin. *Geology. Rev.* 66 (S1), 54–57. doi:10.16509/j.georeview.2020.s1.021

Gao, Z. Q., Fan, T. L., Jiao, Z. F., and Li, Y. (2006b). The Structural Types and Depositional Characteristics of Carbonate Platform in the Cambrian-Ordovician of Tarim Basin. *ACTA Sedimentologica Sinica* 24 (1), 19–27. CNKI:SUN:CJXB.0.2006-01-002.

Gao, Z., and Fan, T. (2015). Carbonate Platform-Margin Architecture and its Influence on Cambrian-Ordovician Reef-Shoal Development, Tarim Basin, NW China. *Mar. Pet. Geology.* 68, 291–306. doi:10.1016/j.marpetgeo.2015.08.033

Gao, Z. Q., Fan, T. L., and Li, Y. (2006a). Study on Eustatic Sea-Level Change Rule in Cambrian Ordovician in Tarim Basin. *J. Jilin Univ. (Earth Sci. Edition)* 36 (4), 549–556. doi:10.13278/j.cnki.jjuese.2006.04.009

Goldstein, R. H. (2001). Fluid Inclusions in Sedimentary and Diagenetic Systems. *Lithos* 55, 159–193. doi:10.1016/s0024-4937(00)00044-x

Goldstein, R. H., and Reynolds, T. (1994). *Systematics of Fluid Inclusions in Diagenetic Minerals*. USA: Society for Sedimentary Geology.

Han, C., Lin, C., Lu, X., Tian, J., Ren, L., and Ma, C. (2019). Petrological and Geochemical Constraints on Fluid Types and Formation Mechanisms of the Ordovician Carbonate Reservoirs in Tahe Oilfield, Tarim Basin, NW China. *J. Pet. Sci. Eng.* 178, 106–120. doi:10.1016/j.petrol.2019.03.010

He, S. L., Zhang, X. B., and Song, M. F. (2020). Multi-Period Denudation Process of the Middle-Lower Ordovician Top Surface and its Relationship with Oil and Gas in the Tabei Area, Tarim Basin. *Chin. J. Geology.* 55 (3), 829–851. doi:10.12017/dzkx.2020.051

Jia, D., Lu, H., Cai, D., Wu, S., Shi, Y., and Chen, C. (1998). Structural Features of Northern Tarim Basin: Implications for Regional Tectonics and Petroleum Traps. *AAPG Bull.* 82 (1), 147–159. doi:10.1306/1d9bc3b3-172d-11d7-8645000102c1865d

Jin, Q., Kang, X., and Tian, F. (2015). Genesis of Chemical Fillings in Fracture-Caves in Paleo-Karst Runoff Zone in Ordovician and Their Distributions in Tahe Oilfield, Tarim Basin. *ACTA Petrolei Sinica* 36 (7), 791–798. doi:10.7623/syxb201507003

Johannesson, K. H., Hawkins, D. L., and Cortés, A. (2006). Do Archean Chemical Sediments Record Ancient Seawater Rare Earth Element Patterns? *Geochimica et Cosmochimica Acta* 70, 871–890. doi:10.1016/j.gca.2005.10.013

Kerans, C. (1988). Karst-Controlled Reservoir Heterogeneity in Ellenburger Group Carbonates of West Texas. *AAPG Bull.* 72 (10), 1160–1183. doi:10.1306/703c996f-1707-11d7-8645000102c1865d

Lawrence, M. G., Greig, A., Collerson, K. D., and Kamber, B. S. (2006). Rare Earth Element and Yttrium Variability in South East Queensland Waterways. *Aquat. Geochem.* 12, 39–72. doi:10.1007/s10498-005-4471-8

Li, F., Webb, G. E., Algeo, T. J., Kershaw, S., Lu, C., Oehlert, A. M., et al. (2019). Modern Carbonate Ooids Preserve Ambient Aqueous REE Signatures. *Chem. Geology.* 509, 163–177. doi:10.1016/j.chemgeo.2019.01.015

Li, K., Cai, C., He, H., Jiang, L., Cai, L., Xiang, L., et al. (2011). Origin of Palaeo-Waters in the Ordovician Carbonates in Tahe Oilfield, Tarim Basin: Constraints from Fluid Inclusions and Sr, C and O Isotopes. *Geofluids* 11, 71–86. doi:10.1111/j.1468-8123.2010.00312.x

Li, Z., Goldstein, R. H., and Franseen, E. K. (2017). Meteoric Calcite Cementation: Diagenetic Response to Relative Fall in Sea-Level and Effect on Porosity and Permeability, Las Negras Area, southeastern Spain. *Sediment. Geology.* 348, 1–18. doi:10.1016/j.sedgeo.2016.12.002

Liu, C. G., Zhang, Y., and Lv, H. T. (2008). Genesis and Evolution of Gigantic Calcites in Paleokarstic Caves of Middle-Lower Ordovician in Tahe Oilfield. *Geol. Sci. Technol. Inf.* 27 (4), 33–38. doi:10.3969/j.issn.1000-7849.2008.04.006

Liu, C., Li, G., Wang, D., Liu, Y., Luo, M., and Shao, X. (2016). Middle-Upper Ordovician (Darriwilian-Early Katian) Positive Carbon Isotope Excursions in the Northern Tarim Basin, Northwest China: Implications for Stratigraphic Correlation and Paleoclimate. *J. Earth Sci.* 27 (2), 317–328. doi:10.1007/s12583-016-0696-2

Liu, L. H., Ma, Y. S., Liu, B., and Wang, C. L. (2017). Hydrothermal Dissolution of Ordovician Carbonates Rocks and its Dissolution Mechanism in Tarim Basin, China. *Carbonates Evaporites* 32, 525–537. doi:10.1007/s13146-016-0309-2

Liu, P.-X., Deng, S.-B., Guan, P., Jin, Y.-Q., Wang, K., and Chen, Y.-Q. (2020). The Nature, Type, and Origin of Diagenetic Fluids and Their Control on the Evolving Porosity of the Lower Cambrian Xiaoerbulak Formation Dolostone, Northwestern Tarim Basin, China. *Pet. Sci.* 17, 873–895. doi:10.1007/s12182-020-00434-0

Liu, Y. L., Luo, M. X., Xia, Y. T., and Shao, X. M. (2017). Geochemical Evidence for Hydrocarbon Accumulation in Deep Ordovician in TS3 Well Block, Tahe Oilfield. *Pet. Geology. Exp.* 39 (3), 377–382. doi:10.11781/sysydz201703377

Lønøy, B., Pennos, C., Tveranger, J., Fikos, I., Vargemezis, G., and Lauritzen, S. E. (2021). Delimiting Morphological and Volumetric Elements of Cave Surveys as Analogues for Paleokarst Reservoir Modelling – A Case Study from the Maaras Cave System, Northern Greece. *Mar. Pet. Geology.* 129, 105091. doi:10.1016/j.marpetgeo.2021.105091

Loucks, R. G. (1999). Paleocave Carbonate Reservoirs: Origins, Burial-Depth Modifications, Spatial Complexity, and Reservoir Implications. *AAPG Bull.* 83 (11), 1795–1834. doi:10.1306/e4fd426f-1732-11d7-8645000102c1865d

Lu, X., Wang, Y., Tian, F., Li, X., Yang, D., Li, T., et al. (2017). New Insights into the Carbonate Karstic Fault System and Reservoir Formation in the Southern Tahe Area of the Tarim Basin. *Mar. Pet. Geology.* 86, 587–605. doi:10.1016/j.marpetgeo.2017.06.023

Lu, Z., Chen, H., Qing, H., Chi, G., Chen, Q., You, D., et al. (2017). Petrography, Fluid Inclusion and Isotope Studies in Ordovician Carbonate Reservoirs in the Shunnan Area, Tarim basin, NW China: Implications for the Nature and Timing of Silicification. *Sediment. Geology.* 359, 29–43. doi:10.1016/j.sedgeo.2017.08.002

Lv, H. T., Zhang, D. J., and Yang, Y. C. (2009). Stage of Paleokastic Hypergenesis in Ordovician Reservoir, Tahe Oilfield. *Geol. Sci. Technol. Inf.* 28 (6), 71–75+83.

Machel, H. G., Cavell, P. A., and Patey, K. S. (1996). Isotopic Evidence for Carbonate Cementation and Recrystallization, and for Tectonic Expulsion of Fluids into the Western Canada Sedimentary Basin. *Geol. Soc. America Bull.* 108 (9), 1108–1119. doi:10.1130/0016-7606(1996)108<1108:iefcca>2.3.co;2

McLennan, S. M. (1989). Rare Earth Elements in Sedimentary Rocks: Influence of Provenance and Sedimentary Processes. *Geochem. Mineralogy Rare Earth Elem. Rev. Mineralogy* 21, 170–200. doi:10.1515/9781501509032-010

Méndez, J. N., Jin, Q., González, M., Zhang, X. D., Lobo, C., Boateng, C. D., et al. (2019). Fracture Characterization and Modeling of Karsted Carbonate Reservoirs: A Case Study in Tahe Oilfild, Tarim Basin (Western China). *Mar. Pet. Geology.* 112, 1–17. doi:10.1016/j.marpetgeo.2019.104104

Menning, D. M., Wynn, J. G., and Garey, J. R. (2015). Karst Estuaries Are Governed by Interactions between Inland Hydrological Conditions and Sea Level. *J. Hydrol.* 527, 718–733. doi:10.1016/j.jhydrol.2015.05.021

Mylroie, J. R., and Mylroie, J. E. (2007). Development of the Carbonate Island Karst Model. *J. Cave Karst Stud.* 69 (1), 59–75. doi:10.1016/j.jseaes.2006.11.004

O'Neil, J. R., Clayton, R. N., and Mayeda, T. K. (1969). Oxygen Isotope Fractionation in Divalent Metal Carbonates. *J. Chem. Phys.* 51 (12), 5547–5558. doi:10.1063/1.1671982

Paton, C., Hellstrom, J., Paul, B., Woodhead, J., and Hergt, J. (2011). Iolite: Freeware for the Visualisation and Processing of Mass Spectrometric Data. *J. Anal. Spectrom.* 26, 2508–2518. doi:10.1039/c1ja10172b

Qi, L. X., and Yun, L. (2010). Development Characteristics and Main Controlling Factors of the Ordovician Carbonate Karst in Tahe Oilfield. *Oil Gas Geology.* 31 (1), 1–12. doi:10.11743/ogg20100101

Raeisi, E., and Mylroie, J. E. (1995). Hydrodynamic Behavior of Caves Formed in the Fresh-Water Lens of Carbonate Islands. *Carbonates Evaporites* 10 (2), 207–214. doi:10.1007/bf03175405

Rossi, C., Goldstein, R. H., Ceriani, A., and Marfil, R. (2002). Fluid Inclusions Record thermal and Fluid Evolution in Reservoir Sandstones, Khatatba Formation, Western Desert, Egypt: A Case for Fluid Injection. *AAPG Bull.* 86 (10), 1773–1799. doi:10.1306/61eedd78-173e-11d7-8645000102c1865d

Sayago, J., Di Lucia, M., Mutti, M., Cotti, A., Sitta, A., Broberg, K., et al. (2012). Characterization of a Deeply Buried Paleokarst Terrain in the Loppa High Using Core Data and Multiattribute Seismic Facies Classification. *AAPG Bull.* 96 (10), 1843–1866. doi:10.1306/02271211137

Shields, G., and Stille, P. (2001). Diagenetic Constraints on the Use of Cerium Anomalies as Palaeoseawater Redox Proxies: An Isotopic and REE Study of Cambrian Phosphorites. *Chem. Geology.* 175, 29–48. doi:10.1016/s0009-2541(00)00362-4

Steele-MacInnis, M., Bodnar, R. J., and Naden, J. (2011). Numerical Model to Determine the Composition of H2O-NaCl-CaCl2 Fluid Inclusions Based on Microthermometric and Microanalytical Data. *Geochimica et Cosmochimica Acta* 75 (1), 21–40. doi:10.1016/j.gca.2010.10.002

Sun, S., Zhao, W., Zhang, B., Liu, J., Zhang, J., and Shan, X. (2013). Observation and Implication of the Paleo-Cave Sediments in Ordovician Strata of Well Lundong-1 in the Tarim Basin. *Sci. China Earth Sci.* 56 (4), 618–627. doi:10.1007/s11430-012-4563-4

Talbot, M. R. (1990). A Review of the Palaeohydrological Interpretation of Carbon and Oxygen Isotopic Ratios in Primary Lacustrine Carbonates. *Chem. Geology. Isotope Geosci. section* 80 (4), 261–279. doi:10.1016/0168-9622(90)90009-2

Tian, F., Jin, Q., Lu, X., Lei, Y., Zhang, L., Zheng, S., et al. (2016). Multi-Layered Ordovician Paleokarst Reservoir Detection and Spatial Delineation: A Case Study in the Tahe Oilfield, Tarim Basin, Western China. *Mar. Pet. Geology.* 69, 53–73. doi:10.1016/j.marpetgeo.2015.10.015

Tian, F. L., He, D. F., Chen, J. J., Ma, D. B., and Huang, C. (2020). Structural Properties of the Mid-Caledonian Movement Surfaces in the Shuntuoguole Lower Uplift and Adjacent Area, Tarim Basin. *Chin. J. Geology.* 55 (3), 813–828. doi:10.12017/dzkx.2020.050

Tostevin, R., Shields, G. A., Tarbuck, G. M., He, T., Clarkson, M. O., and Wood, R. A. (2016). Effective Use of Cerium Anomalies as a Redox Proxy in Carbonate-Dominated marine Settings. *Chem. Geology.* 438, 146–162. doi:10.1016/j.chemgeo.2016.06.027

Ujiie, K., Yamaguchi, A., and Taguchi, S. (2008). Stretching of Fluid Inclusions in Calcite as an Indicator of Frictional Heating on Faults. *Geology* 36 (2), 111–114. doi:10.1130/g24263a.1

Veizer, J., Ala, D., Azmy, K., Bruckschen, P., Buhl, D., Bruhn, F., et al. (1999). 87Sr/86Sr, δ13C and δ18O Evolution of Phanerozoic Seawater. *Chem. Geology.* 161, 59–88. doi:10.1016/s0009-2541(99)00081-9

Webb, G. E., Nothdurft, L. D., Kamber, B. S., Kloprogge, J. T., and Zhao, J.-X. (2009). Rare Earth Element Geochemistry of Scleractinian Coral Skeleton during Meteoric Diagenesis: A Sequence through Neomorphism of Aragonite to Calcite. *Sedimentology* 56, 1433–1463. doi:10.1111/j.1365-3091.2008.01041.x

Wilkinson, J. J. (2017). Metastable Freezing: A New Method for the Estimation of Salinity in Aqueous Fluid Inclusions. *Econ. Geology.* 112 (1), 185–193. doi:10.2113/econgeo.112.1.185

Wu, J., Fan, T., Gomez-Rivas, E., Travé, A., Gao, Z., Wang, S., et al. (2021). Fractal Characteristics of Pore Networks and Sealing Capacity of Ordovician Carbonate Cap Rocks: A Case Study Based on Outcrop Analogues from the Tarim Basin, China. *AAPG Bull.* 105 (2), 437–479. doi:10.1306/03172019022

Yang, X., Wang, X., Tang, H., Ding, Y., Lv, H., and Liu, C. (2014). The Early Hercynian Paleo-Karstification in the Block 12 of Tahe Oilfield, Northern Tarim Basin, China. *Carbonates Evaporites* 29, 251–261. doi:10.1007/s13146-013-0167-0

Zhang, H., Cai, Z., Qi, L., and Yun, L. (2017). Diagenesis and Origin of Porosity Formation of Upper Ordovician Carbonate Reservoir in Northwestern Tazhong Condensate Field. *J. Nat. Gas Sci. Eng.* 38, 139–158. doi:10.1016/j.jngse.2016.12.008

Zhang, S., Jin, Q., Hu, M. Y., Han, Q. C., Sun, J. F., Cheng, F. Q., et al. (2021). Differential Structure of Ordovician Karst Zone and Hydrocarbon Enrichment in Different Paleogeomorphic Units in Tahe Area, Tarim Basin, NW China. *Pet. Exploration Develop.* 48 (5), 1–12. doi:10.1016/s1876-3804(21)60095-2

Zhang, T., Yun, L., Wu, X. W., and Ye, D. S. (2005). The Application of Strontium Isotopes in Division of Paleokarst Stages in Tahe Oilfield. *Pet. Geology. Exp.* 27 (3), 299–303. doi:10.3969/j.issn.1001-6112.2005.03.018

Zhang, W., Guan, P., Jian, X., Feng, F., and Zou, C. N. (2015). *In Situ* geochemistry of Lower Paleozoic Dolomites in the Northwestern Tarim Basin: Implications for the Nature, Origin, and Evolution of Diagenetic Fluids. *Geochem. Geophys. Geosystems* 15 (7), 2744–2764. doi:10.1002/2013GC005194

Zhu, D. Y., Meng, Q. Q., Hu, W. X., and Jin, Z. J. (2013). Differences between Fluids Activities in the Central and North Tarim Basin. *Geochimica* 42 (1), 82–94. doi:10.19700/j.0379-1726.2013.01.008

Conflict of Interest: Authors XH and FX were employed by the company Northwest Oilfield Company Sinopec. Authors XB and XZ were employed by the company PetroChina Southwest Oil and Gasfield Company.

The remaining authors declare that the research was conducted in the absence of any commercial or financial relationships that could be construed as a potential conflict of interest.

Publisher's Note: All claims expressed in this article are solely those of the authors and do not necessarily represent those of their affiliated organizations, or those of the publisher, the editors and the reviewers. Any product that may be evaluated in this article, or claim that may be made by its manufacturer, is not guaranteed or endorsed by the publisher.